Effects of surface-charge regulation, convection, and slip lengths on the electrical conductance of charged nanopores

Yoav Green

Phys. Rev. Fluids **7**, 013702 — Published 25 January 2022

DOI: 10.1103/PhysRevFluids.7.013702

Effects of surface-charge regulation, convection, and slip lengths on the electrical conductance of charged nanopores

Yoav Green*

Department of Mechanical Engineering, Ben-Gurion University of the Negev,

Beer-Sheva 8410501, Israel

* yoavgreen@bgu.ac.il ORCID number: 0000-0002-0809-6575

The electric conductance characterizes the response of a nanochannel/nanopore to an electrical potential drop. It has long been known that at low concentrations the electric conductance is independent of the bulk electrolyte concentration but depends on the surface charge density. In recent years, several works have demonstrated that the low-concentration conductance is concentration-dependent. This dependence is implicit through the mechanism known as surface charge regulation which causes the surface charge density to depend on the concentration, $\tilde{c}_0$. As a result, the conductance, $\tilde{G}$, has power-law dependency such that $\tilde{G} \sim \tilde{c}_0^{\alpha}$ with a slope of α. It is typically assumed the slope takes on the particular values $\alpha = 0, \frac{1}{3}, \frac{1}{2}$. Here, we will analytically show that slope varies continuously from 0 to $\frac{1}{2}$ as the system parameters vary. Thereafter, we will account for convection and the effects of a slip length at the channel surface. We will show that convection without slip increases the conductance but does not vary the slope α. The inclusion of slip not only increases the conductance but also increases the slope to 2α. Direct numerical simulations confirm our theoretical predictions. The consequences of these findings are important in the design of any electro-kinetically driven nanofluidic system insofar as they provide the experimentalist an accurate prediction of the system response as a function of the material properties.

I. INTRODUCTION

The discovery of new materials and the development of more advanced fabrication methods results in system sizes that are ever decreasing [1]. With this comes the potential to enhance our understanding of nanoscale physics and, in parallel, revolutionize current technological setups. Of particular interest is the transport of ions across these nanoscale systems. Nanochannels, nanotubes, nanopores, and nanoporous materials are ubiquitous to nature and technology. They are found in desalination [2–7] and energy harvesting [8–21] systems, as well as biosensing [22–29], fluid-based electrical diodes [30–41], and various physiological phenomena [42–45]. However, as pointed out in recent reviews [7–9,46–48], numerous challenges related to scalability, fabrication technology, and elucidation of the unknown fundamental physics at these small scales remain. Specifically, it is known that a plethora of mechanisms, unique to nanoscale systems, determine the system's overall response. Many of these mechanisms have already been investigated separately. However, the interplay of these mechanisms is not fully understood. This work will address how the interplay of surface charge regulation, bulk convection, and hydrodynamic slip length varies nanopore systems' conductance.

The electrical conductance, $\tilde{G}$, is the ratio of the electrical current, $\tilde{I}$, to the electrical potential drop, $\tilde{V}$ (i.e. $\tilde{G} = \tilde{I} / \tilde{V}$). In contrast, to classical metallic conductors (i.e., the Drude model), whose response is typically linear with the number density (i.e., the concentration of electrons) [49], electrolyte-based conductors display more complicated behavior. This can be associated with fluid-structure interactions – namely, the charging of the electric double layer (EDL), surface charge regulation, convection, slip lengths, and more.

Stein et al.'s [50] pioneering work showed that the Ohmic conductance behaved peculiarly. At high bulk concentrations, $\tilde{c}_0$, when the electric double layers (EDLs)

$$\tilde{\lambda}_D = \sqrt{\frac{\tilde{\varepsilon}_0 \varepsilon_r \tilde{R}_g \tilde{T}}{2\tilde{F}^2 z^2 \tilde{c}_0}}, \quad (1)$$

do not overlap (i.e., the EDL is much smaller than the pore radius, $\tilde{a}$, such that $\tilde{\lambda}_D \ll \tilde{a}$), the conductance increases linearly with the bulk concentration ($\tilde{G}_{high} \sim \tilde{c}_0$). Here $\tilde{R}_g$ is the universal gas constant, $\tilde{T}$ is the temperature, $\tilde{F}$ is the Faraday constant, and $\tilde{\varepsilon}_0$ and ε_r are the permittivity of free space and the relative permittivity, respectively. At low concentrations, when the EDLs overlap ($\tilde{\lambda}_D \gg \tilde{a}$) and the effects of the surface charge are prominent , the conductance saturates to a constant value that is independent of the concentration but depends on the surface charge density, $\tilde{\sigma}_s$, such that $\tilde{G}_{low} \sim \tilde{\sigma}_s$. The thick dashed orange line in **Figure 1** depicts the behavior schematically and is given by the well-known equation [51–53]

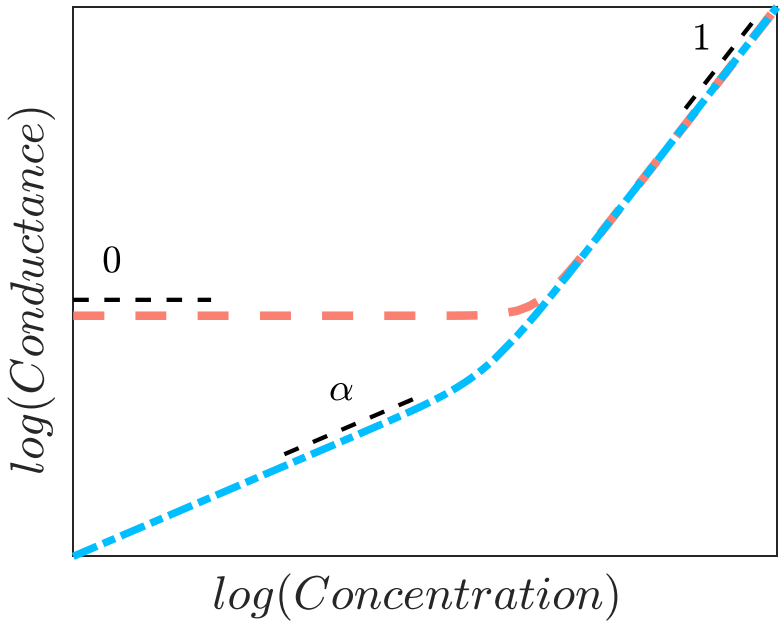

Figure 1. Schematic behavior of the linear Ohmic conductance, G, of a long nanopore versus the bulk concentration, c_0. The slopes are denoted by the numbers above the thin dashed black lines. The variation of the slope α at low concentrations is discussed throughout this work.

$$\tilde{G}_{Ohmic} = \tilde{\kappa}_{cond}\sqrt{4+\left(\frac{\tilde{N}}{\tilde{c}_0}\right)^2}\,\frac{\pi\tilde{a}^2}{\tilde{L}}, \tag{2}$$

where κ_{cond} is the conductivity

$$\tilde{\kappa}_{cond} = z^2\tilde{F}^2\tilde{D}\tilde{c}_0/(\tilde{R}_g\tilde{T}), \tag{3}$$

$\tilde{a}$ is the pore radius, $\tilde{L}$ is the pore length, and $\tilde{D}$ is the diffusion coefficient. Here $\tilde{N}$ represents the average excess counterion concentration due to the surface charge density [derived later in Eq. (36) and again in Appendix A]

$$\tilde{N} = -\frac{2\tilde{\sigma}_s}{\tilde{a}\tilde{F}z}, \tag{4}$$

and it is explicitly independent of the concentration. Equation (2) is *typically* derived under numerous assumptions: that convection is negligible, the electrolyte is symmetric (defined below), large aspect ratio ($\tilde{L}/\tilde{a} \gg 1$), the surface charge density is independent of electrolyte concentrations, and the effects of access-resistances/field-focusing-resistances due to the adjacent microchannels/reservoirs are negligible. We will review and revisit these assumptions throughout this work. In Appendix A, we derive this equation whereby the notation used in Appendix A is provided throughout this work. It is recommended to read this Appendix after Sec. IV.A.

We consider Eq. (2) at the two extreme cases of high and low concentrations. At high concentrations, $\tilde{N} \ll \tilde{c}_0$, the conductance reduces to a term that is linear with the concentration, $\tilde{G}_{Ohmic,high} \sim \tilde{\kappa}_{cond} \sim \tilde{c}_0$ such that the slope is 1 (**Figure 1**). In contrast, at low concentrations, $\tilde{N} \gg \tilde{c}_0$, one finds that the conductance

$$\tilde{G}_{Ohmic,low} = \frac{\tilde{\kappa}_{cond}}{\tilde{c}_0}\left|\tilde{N}\right|\frac{\pi\tilde{a}^2}{\tilde{L}} \sim \tilde{N}\,\frac{\pi\tilde{a}^2}{\tilde{L}}, \tag{5}$$

is explicitly concentration-independent. However, recent works [54–58] have suggested that if the surface charge is regulated, this leads to $\tilde{N} \sim \tilde{c}_0^{\alpha}$. Here, α is the exponent of the power-law dependency of the surface-charge regulation (Sec. III). As a result, Eq. (5) [and Eq. (2)] is implicitly concentration-dependent such that $\tilde{G}_{Ohmic,low} \sim \tilde{c}_0^{\alpha}$ and the slope is no longer zero, but rather it is α. The dotted-dashed blue line in **Figure 1** denotes Eq. (2) under the assumption of charge regulation.

This work is structured as follows. In Sec. II, we introduce the model and governing equations. After which, we derive the solutions for fully developed profiles. We then calculate the transport coefficients, which represent the various contributions to the conductance. Before we analyze these coefficients, in Sec. III, we derive an expression for the surface density under the assumption of surface charge regulation whereby we show that the surface charge density varies with the conditions of the environment (namely the concentration and more). In Sec. IV, we analyze the transport coefficients and their dependence on the various system parameters (including space charge regulation, slip lengths, and more). The discussion and conclusions are presented in Sec. V. Throughout this work, we compare our theoretical predictions with numerical simulations. The correspondence is outstanding.

II. MODEL AND SOLUTION DERIVATION

This section is divided into six parts. First, in Sec. II.A, we present the geometry of the system and discuss the composition of the electrolyte. In Sec. II.B, we present the governing equations and the normalizations. In Sec. II.C, we derive the solution for the concentration and electric potential distributions while in Sec. II.D we derive the axial velocity distribution. Section II.E presents a comparison of the theoretical results of the two previous sub-sections to numerical simulations. In Sec. II.F, we calculate the transport coefficients – namely the various contributions to the conductance. These contributions are analyzed in Sec. IV.

A. Geometry and electrolyte components

In this work, we model a cylinder of length $\tilde{L}$ and radius $\tilde{a}$ with a surface charge density, $\tilde{\sigma}_s$ as shown in **Figure 2**(a). Dimensional quantities are denoted with tildes, while non-dimensional quantities are without tildes. The various normalizations are discussed and provided below [Sec. II.B]. Shortly, we will assume that the length is substantially longer than the radius, $\tilde{L}/\tilde{a} \gg 1$, such that all the distributions are fully developed.

Figure 2 schematically depicts ions within a negatively charged pore. In the figure, we have added only the two major charge carriers of the salt (for example K_+ and Cl_-). In reality, there are at least two additional species – these are H_+ and OH_-. In the following, we explicitly assume that the concentration, electric potential, and velocity profiles are determined by two of these species alone – these are the main charge carriers – which we assume to be symmetric such as, K_+ and Cl_-. In a realistic electrolyte, there is always a presence of H_+ and OH_-. However, their concentration is typically small enough that they are not dominant. In fact, due to coion exclusion, the concentration of OH_- is substantially smaller than that of H_+, to the point that we will not mention OH_- further. In contrast, while H_+ does not directly influence the system response, it indirectly regulates the surface charge density. The topic of surface charge regulation is discussed in Sec. III. In the following derivation, we do not directly model the effects of H_+ and OH_-.

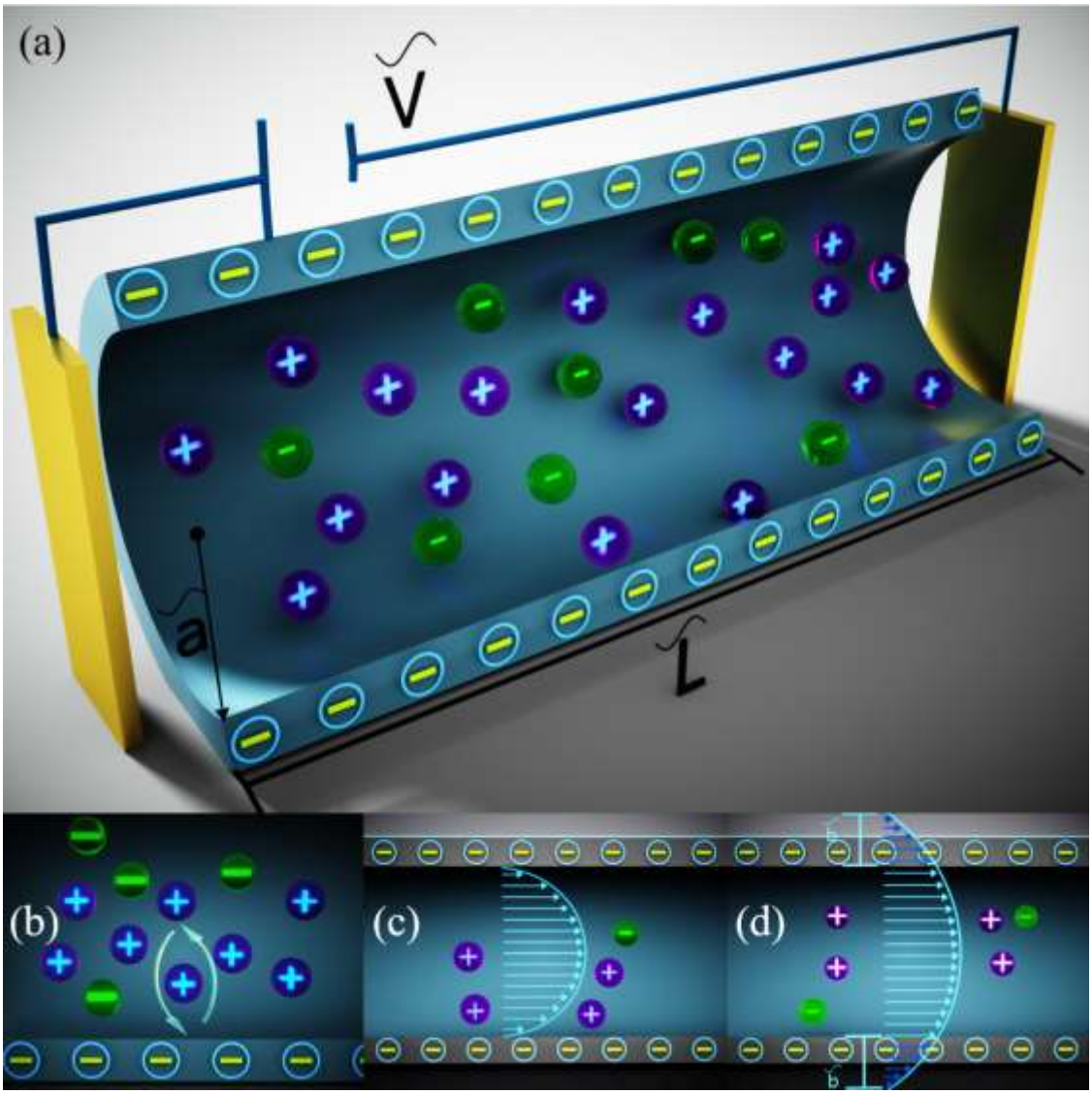

Figure 2. (a) Schematic representation of a negatively charged long nanotube ($L \gg a$). Due to the negative surface charge density, σ_s, there is an excess of positive counterions, represented by purple spheres, over the negative coions, represented by green spheres. This work focuses on the case of a highly selective channel $(\varepsilon = \tilde{\lambda}_D / \tilde{a} \gg 1)$ which corresponds to the case of few negative ions. (b) The surface charge density is regulated by H_+ and OH_- (discussed in the text). A schematic profile of a (c) no-slip velocity profile and (d) a velocity profile with a slip length $\tilde{b}$. All three mechanisms [(b)surface charge regulation, (c) bulk convection, and (d) slip lengths) vary the conductance.

B. Governing equations

The non-dimensional steady-state equations that govern ion transport in a system with a symmetric binary electrolyte with equal diffusion coefficients ($\tilde{D}_{\pm} = \tilde{D}$) and opposite valences ($z_{\pm} = \pm z$) are the Nernst-Planck-Poisson-Stokes (PNP-S)equations

$$-\nabla \cdot \mathbf{j}_{\pm} = \nabla \cdot (\nabla c_{\pm} \pm c_{\pm} \nabla \vartheta) - \mathrm{Pe}(\mathbf{u} \cdot \nabla c_{\pm}) = 0\,, \tag{6}$$

$$2\varepsilon^2 \nabla^2 \vartheta = -(c_+ - c_-)\,, \tag{7}$$

$$\nabla \cdot \mathbf{u} = 0\,, \tag{8}$$

$$\nabla^2 \mathbf{u} + \nabla^2 \vartheta \nabla \vartheta = 0\,. \tag{9}$$

Here we have assumed that the pressure gradient in Stokes equation [Eq. (9)] is zero, and we have used the following normalizations

$$\tilde{\mathbf{r}} = \tilde{a}\mathbf{r},\ \tilde{\vartheta} = \tilde{\vartheta}_{th}\vartheta,\ \tilde{c}_{\pm} = c_{\pm}\tilde{c}_0,\ \tilde{\mathbf{j}}_{\pm} = \tilde{j}_0 \mathbf{j}_{\pm},\ \tilde{\mathbf{u}} = \tilde{u}_0 \mathbf{u}\,. \tag{10}$$

The spatial coordinates are normalized by the radius, $\tilde{a}$. The electric potential, ϑ, has been normalized by the thermal potential, $\tilde{\vartheta}_{th} = \tilde{R}_g \tilde{T} / \tilde{F} z$, where $\tilde{R}_g$ is the universal gas constant, $\tilde{T}$ is the temperature, and $\tilde{F}$ is the Faraday constant. The concentrations, $c_{\pm}$, have been normalized by the bulk concentrations $\tilde{c}_0$. These normalizations lead to the non-dimensional Debye length or non-dimensional electric double layer (EDL)

$$\varepsilon = \frac{\tilde{\lambda}_D}{\tilde{a}} = \frac{1}{\tilde{a}} \sqrt{\frac{\tilde{\varepsilon}_0 \varepsilon_r \tilde{R}_g \tilde{T}}{2\tilde{F}^2 z^2 \tilde{c}_0}}\,, \tag{11}$$

where $\tilde{\varepsilon}_0$ and ε_r are the permittivity of free space and the relative permittivity. The normalizations of Eq. (10) also lead to natural scales for the fluxes, $\mathbf{j}_{\pm}$, and the velocity, $\mathbf{u}$. These are respectively $\tilde{j}_0$ and $\tilde{u}_0$

$$\tilde{j}_0 = \tilde{c}_0 \tilde{D} / \tilde{a},\ \tilde{u}_0 = \tilde{\varepsilon}_0 \varepsilon_r \tilde{\varphi}_{th}^2 / \tilde{\mu}\tilde{a}\,, \tag{12}$$

where $\tilde{\mu}$ is fluid's viscosity. Notably, the Peclet number, which is the non-dimensional number ratio of convective fluxes to diffusive fluxes, arises. Here, the Peclet number is defined as

$$\mathrm{Pe} = \frac{\tilde{u}_0 \tilde{a}}{\tilde{D}} = \frac{\tilde{\varepsilon}_0 \varepsilon_r \tilde{\varphi}_{th}^2}{\tilde{\mu} \tilde{D}}. \tag{13}$$

In Sec. II.F, we will demonstrate the contributions of the convective fluxes to the conductance via the dependence on Pe.

We assume that the channel has a large aspect ratio, $L/a \gg 1$. As a result, derivatives of the fluxes in the axial direction are negligible such that $\partial_x = 0$. Further, we assume axisymmetric profiles whereby derivatives in the azimuthal direction are zero, $\partial_\theta = 0$. As a result, the equations depend solely on the radial coordinate, r. The large aspect ratio also allows the electric potential to be separated into two terms

$$\vartheta(r,x) = \varphi(r) + V(1 - x/L). \tag{14}$$

The first term represents the electric potential of the fully developed profile. The second term represents the linear Ohmic potential drop across a channel of length L due to a voltage drop of V. In the remainder of this work, we will also denote the thermal potential in Eq. (10) as $\tilde{\vartheta}_{th} = \tilde{\varphi}_{th}$. Also, it should become evident that the electric field in the axial direction is given by the constant (the subscript of a comma denotes a derivative)

$$E = -\vartheta_{,x} = V/L. \tag{15}$$

C. Potential and concentration solutions

For fully developed and axisymmetric profiles, the Nernst-Plank [Eq. (6)] and Poisson equations [Eq. (7)] are drastically simplified

$$c_{\pm,r} \pm c_\pm \varphi_{,r} = 0, \tag{16}$$

$$2\varepsilon^2 r^{-1}(r\varphi_{,r})_{,r} = -(c_+ - c_-). \tag{17}$$

Note that Eq. (16) has assumed that there is no flux into the solid wall

$$\mathbf{j}_{\pm}(r=1)\cdot\hat{\mathbf{r}}=0. \tag{18}$$

Integrating Eq. (16) leads to

$$c_{\pm}=e^{\mp\varphi}. \tag{19}$$

Substituting Eq. (19) into Eq. (17) yields the Poisson Boltzmann (PB) equation [59]

$$2\varepsilon^2 r^{-1}(r\varphi_{,r})_{,r}=-(e^{-\varphi}-e^{\varphi}). \tag{20}$$

To solve the PB equation, we supplement the boundary conditions of no flux at the center of the channel and a surface charge density at the surface of the channel, respectively,

$$\varphi_{,r}(r=0)=0, \tag{21}$$

$$\varphi_{,r}(r=1)=\sigma_s, \tag{22}$$

where the dimensional-less surface charge density has been normalized by

$$\tilde{\sigma}_d=\tilde{\varepsilon}_0\varepsilon_r\tilde{\varphi}_{th}/\tilde{a}, \tag{23}$$

(i.e. $\sigma_s=\tilde{\sigma}_s/\tilde{\sigma}_d$). Here, we assume that the surface charge is negative (i.e. $\sigma_s<0$). Shortly, this will lead to coion exclusion of negatively charged ions.

For the case of highly overlapping EDLs ($\varepsilon\gg1$), with a surface charge of order unity [$|\sigma_s|\sim O(1)$], Schnitzer and Yariv [60] suggest a solution of the form

$$\varphi=-2\ln\varepsilon+\phi. \tag{24}$$

Substituting Eq. (24) into Eq. (19), combined with $\sigma_s<0$, yields a ratio of the coion to the counterion concentration that is $c_-/c_+\sim O(\varepsilon^{-4})$ [58]. Since $\varepsilon\gg1$, we conclude that the effects of the coions are negligible. Thus, the PB equation is further reduced to

$$r^{-1}(r\phi_{,r})_{,r}=-\tfrac{1}{2}e^{-\phi}. \tag{25}$$

The solution of this equation is [56–58,61,62]

$$\varphi = \ln\left\{\frac{[4+(r^2-1)\sigma_s]^2}{16\sigma_s(\sigma_s-4)\varepsilon^2}\right\}, \tag{26}$$

$$c_+ = e^{-\varphi} = \frac{16\sigma_s(\sigma_s-4)}{[4+(r^2-1)\sigma_s]^2}\varepsilon^2 . \tag{27}$$

D. Solution: Velocity distributions

For unidirectionally developed flows, the simplified governing equation for the velocity field in the axial direction is

$$r^{-1}(ru_{x,r})_{,r} + r^{-1}(r\vartheta_{,r})_{,r}\vartheta_{,x} = 0 . \tag{28}$$

The appropriate boundary conditions are

$$u_{x,r}(r=0) = 0 , \tag{29}$$

$$u_x(r=1) = -bu_{x,r} . \tag{30}$$

Equation (29) is a symmetry condition at the center of the channel, while Eq. (30) is a slip length boundary condition at the wall. The non-dimensional slip length is normalized by the radius such that $b = \tilde{b}/\tilde{a}$. For $b = 0$, the traditional no-slip boundary condition is recovered. The inclusion of the slip length is new relative to our recent work [58]. We will shortly demonstrate that the slip length is responsible for changing the slope of the conductance. The minus sign in Eq. (30) denotes that the normal to the surface is in the decreasing radial direction.

Equations (28)-(30) are solved via direct integration. Since the governing equation and boundary conditions are linear, the velocity profile can be divided into two contributions: electric body force with a no-slip contribution and a slip contribution

$$u_x = u_{no-slip} + u_{slip} , \tag{31}$$

$$u_{no-slip} = 2E\ln[1+\tfrac{1}{4}(r^2-1)\sigma_s], \tag{32}$$

$$u_{slip} = -b\sigma_s E . \tag{33}$$

Equation (32) has been derived in past works Ref. [56–58,61] while Eq. (33) has also been derived in past works [57,63–65]. However, the dependency of σ_s on the concentration is either overlooked or over-simplified. Thus, the main finding of this work, which is discussed in Sec. IV, is the demonstration of the universal change of the conductance and the slope due to the two terms in Eq. (31).

E. Concentration, electric potential, and velocity plots

In Sec. II.F, we will calculate cross-sectional averages of the various flux contributions – these will include multiplication of the concentration, c_+, with the electric field, E, and the axial velocity, u_x. Therefore, it is useful to compare our theoretically predicted values with those calculated from numerical simulations. The details of the 2D numerical simulations that don't assume fully developed profiles are provided in Appendix B.

Figure 3(a)-(c) compare our theoretical predictions for the fully developed profiles to direct numerical simulations for (a) c_+, (b) ϑ, and (c) u_x at $x = \frac{1}{2}L$. **Figure 3**(d) presents the axial potential distribution on the centerline [i.e. $\vartheta(r = 0, x)$]. The correspondence is excellent, confirming our underlying assumptions and our derivation are self-consistent and correct. The electric potential φ shown in **Figure 3**(b) accounts for the additional $\frac{1}{2}V$ term provided in Eq. (14). In **Figure 3**(d), the edges of the simulation domain have been cropped – these are regions where there are sharps drops in the potential due to the EDLs (i.e., edge effects).

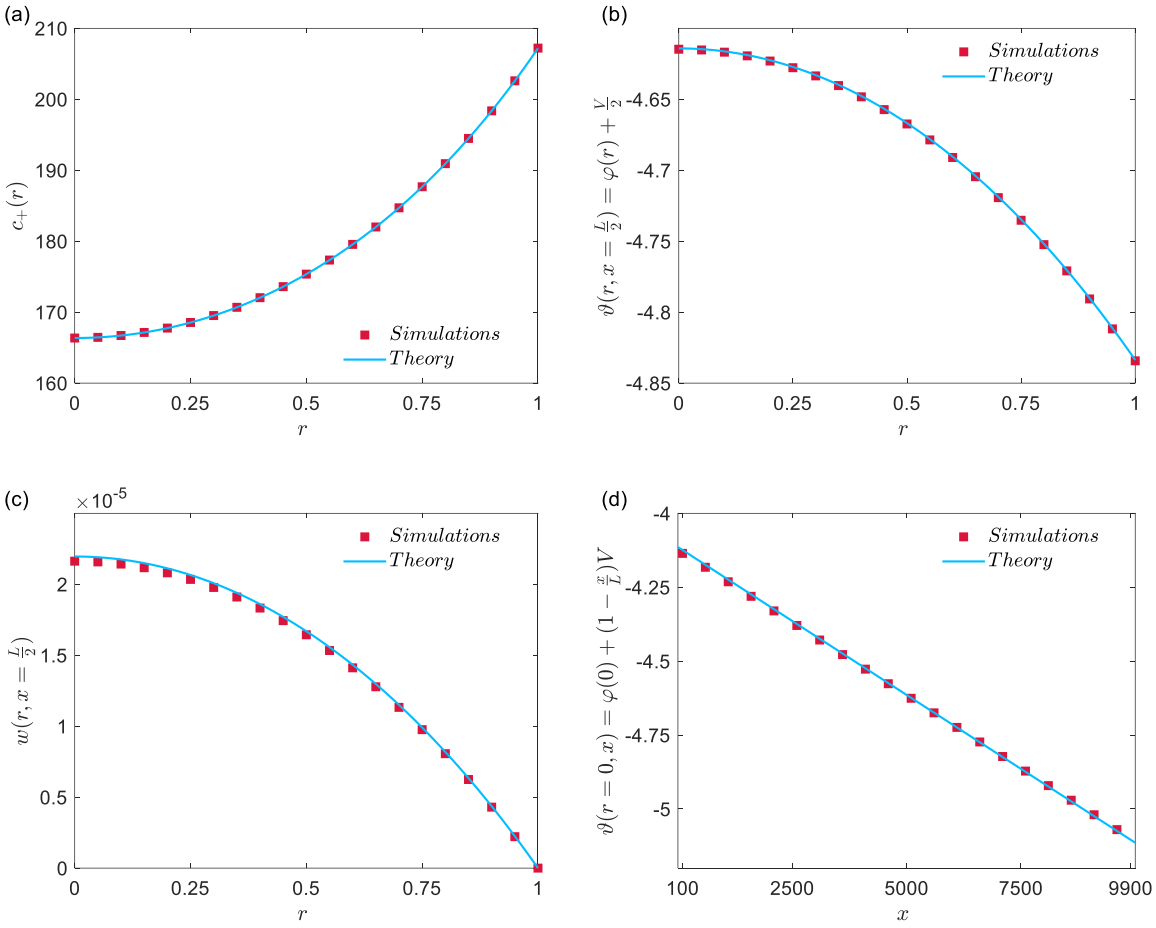

Figure 3. Plots of the (a) concentration [Eq. (27)], (b) electric potential [Eq. (26)], and (c) axial velocity [Eq. (31)] distributions versus the radial coordinate at the center of the channel ($x = L/2$). (d) The electrical potential along the axis ($r = 0$). For presentation purposes, we have presented only some of the simulation points. The simulation parameters are $\varepsilon = 10$, $\sigma_{s,\frac{1}{3}} = -(10/\varepsilon^2)^{1/3}$, $V = 1$, $\mathrm{Pe} = 0.45$, and $b = 0$.

F. Transport coefficients

In non-dimensional units, the cross-sectional average for any quantity f can be calculated by

$$\overline{f} = \frac{1}{\pi}\int_0^{2\pi}\left(\int_0^1 f(r) r dr\right) d\theta = 2\int_0^1 f(r) r dr, \tag{34}$$

where the overbar denotes cross-sectional averages. Here, we will calculate a couple of interesting quantities to confirm our solution. However, our primary focus is on the fluxes/conductance terms.

256 The average counterion concentration is

257 $$N = \overline{c}_+ = 2\int_0^1 crdr = -4\sigma_s\varepsilon^2 . \quad (35)$$

258 In dimensional units, this is

259 $$\tilde{N} = \tilde{\overline{c}}_+ = -\frac{4\tilde{\sigma}_s\varepsilon^2\tilde{c}_0}{\tilde{\sigma}_0} = -\frac{2\tilde{\sigma}_s}{\tilde{a}\tilde{F}z} = -\frac{(2\pi\tilde{a})\tilde{\sigma}_s}{(\pi\tilde{a}^2)\tilde{F}z}, \quad (36)$$

260 which is the expected result one gets if the surface charge density is multiplied by the perimeter
261 and divided by the cross-section area. This is the average excess counterion concentration
262 discussed in the Introduction [and in Eq. (2)]. Note that EDL overlap alone does not guarantee
263 high selectivity. Instead, one must require a combination of surface-charge and EDL effects –
264 namely, the requirement is that $N \gg 1$ [or $\tilde{N} \gg \tilde{c}_0$]. See Appendix A for a short discussion on
265 this issue. Also, the issue of high selectivity versus vanishing selectivity has been extensively
266 discussed in our recent work [66]. Finally, we note that $\tilde{N}$ can be rewritten in terms of the
267 dimensional and non-dimensional Dukhin length, respectively,

268 $$\tilde{l}_{Du} = -\tilde{\sigma}_s / (\tilde{F}\tilde{c}_0), \quad (37)$$

269 $$l_{Du} = -2z\sigma_s\varepsilon^2, \quad (38)$$

270 such that

271 $$\tilde{N} = 2\frac{\tilde{l}_{Du}}{\tilde{a}}\frac{\tilde{c}_0}{z} = 2l_{Du}\frac{\tilde{c}_0}{z} . \quad (39)$$

272 Note that dividing Eq. (39) by $\tilde{c}_0$ yields

273 $$N = 2l_{Du}z^{-1} . \quad (40)$$

274 In the remainder, we will use the notation of N rather than the notation of l_{Du}. However, they
275 are trivially linked through Eq. (40). Also, one can easily note that the two limits of Eq. (2) of
276 $N \ll 1$ and $N \gg 1$ correspond to $l_{Du} \ll 1$ and $l_{Du} \gg 1$, respectively.

The average electrical potential is

$$\bar{\varphi} = 2\int_0^1 \varphi r dr = -2\ln\varepsilon - 2 + \frac{8}{\sigma_s}\ln\left(\frac{4}{\sigma_s - 4}\right) + \ln\left(\frac{\sigma_s - 4}{16\sigma_s}\right). \tag{41}$$

In our previous work [58], we reported, "For the case of large surface charge, which is typically the case in highly selective nanopores, the limit $\sigma_s \to -\infty$, the leading order term is $\bar{\varphi} = -\ln(-4\sigma_s\varepsilon^2) = -\ln\bar{c}_+$." This statement is incorrect, and we wish to correct our miscalculation. In the limit $\sigma_s \to -\infty$, the correct value is given by $\bar{\varphi} = -2 - \ln(16\varepsilon^2)$ which is independent of the surface charge.

Due to coion exclusion, the current is transported solely by the counterions. Thus, the current density in the axial direction is given by

$$i = \mathbf{j}_+ \cdot \hat{\mathbf{x}} = -(c_+\varphi_{,z} - \mathrm{Pe}u_x c_+) = i_{ohmic} + i_{adv}\,. \tag{42}$$

We calculate the average electrical current density of both the ohmic and advective current densities [using Eqs. (26), (27), (15), (31), (34)]. The Ohmic current is

$$\bar{i}_{Ohmic} = 2\int_0^1 c_+ E r dr = \bar{c}_+ E = -4\sigma_s\varepsilon^2\frac{V}{L}. \tag{43}$$

The axial velocity [Eq. (31)] has two contributions: no-slip and slip. Thus, the advective current, too, has two contributions

$$i_{adv} = \mathrm{Pe}c_+ u_x = \mathrm{Pe}c_+(u_{no-slip} + u_{slip}) = i_{adv,no-slip} + i_{adv,slip}\,. \tag{44}$$

We calculate the average of each term

$$\bar{i}_{adv,no-slip} = 2\mathrm{Pe}\int_0^1 c_+ u_{no-slip} r dr = -8\varepsilon^2\mathrm{Pe}[\sigma_s + 4\ln(1 - \tfrac{1}{4}\sigma_s)]\frac{V}{L}, \tag{45}$$

$$\bar{i}_{adv,slip} = 2\mathrm{Pe}\int_0^1 c_+ u_{slip} r dr = 4\mathrm{Pe}b\varepsilon^2\sigma_s^2\frac{V}{L}. \tag{46}$$

Note that Eqs. (43),(45)-(46) are linear with the applied potential drop, V.

297 Consider the conductance, which is the ratio of the current to the voltage

298 $$\bar{G}_{cond} = \bar{i} / V \,. \tag{47}$$

299 Due to the linearity of Eq. (42), the conductance is a sum of three different terms

300 $$\bar{G}_{cond} = \bar{G}_{ohmic} + \bar{G}_{adv,no-slip} + \bar{G}_{adv,slip} \,, \tag{48}$$

301 where

302 $$\bar{G}_{Ohmic} = \frac{\bar{i}_{Ohmic}}{V} = \frac{1}{V}\bar{c}_{+}\frac{V}{L} = \frac{\bar{c}_{+}}{L} = \frac{-4\sigma_s\varepsilon^2}{L} \,, \tag{49}$$

303 $$\bar{G}_{adv,no-slip} = \frac{\bar{i}_{adv,no-slip}}{V} = \frac{-8\varepsilon^2 \mathrm{Pe}\left[\sigma_s + 4\ln(1-\frac{1}{4}\sigma_s)\right]}{L} \,, \tag{50}$$

304 $$\bar{G}_{adv,slip} = \frac{\bar{i}_{adv,slip}}{V} = \frac{4\mathrm{Pe}b\varepsilon^2\sigma_s^2}{L} \,. \tag{51}$$

305 Eqs. (48)-(51) are the non-dimensional expressions for the conductance. Note that two of the
306 terms depend on the Peclet number.

307 The dimensional expressions are recovered by using the normalizations given in Eqs. (10)
308 -(13). The dimensional conductance is related to the non-dimensional conductance

309 $$\tilde{\bar{G}}_{cond} = \bar{G}_{cond}(\tilde{i}_0 / \tilde{\varphi}_{th}) \,, \tag{52}$$

310 where $\tilde{i}_0$ is the characteristic electrical current density given by

311 $$\tilde{i}_0 = z\tilde{F}\tilde{j}_0 = z\tilde{F}\tilde{D}\tilde{c}_0 / \tilde{a} \,. \tag{53}$$

312 The current density to thermal voltage ratio in Eq. (52) is

313 $$\frac{\tilde{i}_0}{\tilde{\varphi}_{th}} = \frac{z\tilde{F}\tilde{D}\tilde{c}_0 / \tilde{a}}{\tilde{R}_g\tilde{T} / \tilde{F}z} = \frac{z^2\tilde{F}^2\tilde{D}\tilde{c}_0}{\tilde{R}_g\tilde{T}}\frac{1}{\tilde{a}} = \frac{\tilde{\kappa}_{cond}}{\tilde{a}} \,, \tag{54}$$

314 where, once more,

315 $$\tilde{\kappa}_{cond} = z^2\tilde{F}^2\tilde{D}\tilde{c}_0 / (\tilde{R}_g\tilde{T}) \,, \tag{55}$$

is the dimensional conductivity. Note that the $\tilde{a}$ in the denominator of Eq. (54) will transform the L in each of the conductance terms to be $\tilde{L}$. After multiplying by the area, $\pi\tilde{a}^2$, the dimensional cross-sectional integrated conductances are

$$\tilde{G}_{Ohmic} = -4\tilde{\kappa}_{cond}\varepsilon^2 \frac{\tilde{\sigma}_s}{\tilde{\sigma}_d}\frac{\pi\tilde{a}^2}{\tilde{L}}, \tag{56}$$

$$\tilde{G}_{adv,no-slip} = -8\tilde{\kappa}_{cond}\varepsilon^2 \mathrm{Pe}\left[\frac{\tilde{\sigma}_s}{\tilde{\sigma}_d} + 4\ln\left(1-\frac{1}{4}\frac{\tilde{\sigma}_s}{\tilde{\sigma}_d}\right)\right]\frac{\pi\tilde{a}^2}{\tilde{L}}, \tag{57}$$

$$\tilde{G}_{adv,slip} = 4\tilde{\kappa}_{cond}\mathrm{Pe}\frac{\tilde{b}}{\tilde{a}}\varepsilon^2\left(\frac{\tilde{\sigma}_s}{\tilde{\sigma}_d}\right)^2\frac{\pi\tilde{a}^2}{\tilde{L}}, \tag{58}$$

$$\tilde{G}_{cond} = \tilde{G}_{ohmic} + \tilde{G}_{adv,no-slip} + \tilde{G}_{adv,slip}. \tag{59}$$

The overbar for the dimensional quantities has been omitted to avoid a complicated notation but also because these are no longer cross-sectional averaged quantities – rather, they are cross-sectional integrated quantities.

Multiplying Eqs. (11) and (55) yields

$$\tilde{\kappa}_{cond}\varepsilon^2 = \frac{\tilde{\varepsilon}_0\varepsilon_r\tilde{D}}{2\tilde{a}^2}, \tag{60}$$

where it can be observed that $\tilde{\kappa}_{cond}\varepsilon^2$ is concentration-independent. This observation will be used in Sec. IV. Before analyzing the behavior of the conductance (Sec. IV), we will now discuss the effects of surface charge regulation (Sec. III).

It is worthwhile to note that the relations given by Eqs. (56)-(59) are very similar to the conductance expression derived in Manghi et al. [57] [their Eq. (19)]. However, several precautionary remarks are needed in comparing this work to Ref. [57]. To compare their low concentration theoretical model to experiments at both low and high concentrations, Manghi et al. [57] attempt to derive a solution that holds for all concentrations (high and low concentrations). To that end, they use an interpolating function to empirically extend their

337 solution from high selectivity [which they term the good-ion exclusion limit (GCE)] to low
338 concentrations. However, such an extension is artificial and is empirical. It is equivalent to
339 assuming a known solution to the Poisson-Boltzmann equation that holds for all concentrations.
340 However, to the best of our knowledge, a tractable analytical solution of the Poisson-
341 Boltzmann equation is unknown except for the two limiting cases of high-selectivity and
342 vanishing selectivity. Thus that extension, and the final form of their Eq. (19), is not rigorous
343 in the sense that it cannot be derived directly from the PNP equations. In fact, in the case that
344 advection is neglected, one would expect that the solution of Manghi et al. [57] would match
345 the well know model of Eq. (2) that is rigoursly derived in Appendix A. It does not. This is yet
346 another indicatation that their interpolation formula is incorrect. In fact, using an interpolation
347 formula to fit two knowns limits is related to the commonly used superposition approach of
348 adding the bulk conductance and the surface charge conductance. In two of our past
349 works [67,68], we have discussed the flaws of the superpositon approach and why it is
350 inapplicable. Those understandings carry over to the "interpolation" approach.

351 In continuation, Manghi et al. [57] introduce another conceptual error regarding their
352 artificial extension of the advective flux. They assume that the advective flux obtained at high
353 selectivity also holds for vanishing selectivity. Vanishing selectivity is derived under the
354 Debye–Hückel (DH) approximation, whose inherent assumption of small potential contradicts
355 the one used here of large potentials. Under the DH approximation, the resultant potential,
356 space-charge density, and no-slip velocity field are given by

357 $$\varphi_{DH} = \varepsilon\sigma_s \frac{I_0(r/\varepsilon)}{I_1(\varepsilon^{-1})}, \tag{61}$$

358 $$\rho_{DH} = -2\varphi_{DH}, \tag{62}$$

359 $$u_{DH} = \varepsilon\sigma_s E \frac{I_0(r/\varepsilon) - I_0(\varepsilon^{-1})}{I_1(\varepsilon^{-1})}. \tag{63}$$

It is evident that all these distributions are different than those of highly-selective systems. We see that the space charge for the DH approximation, given by Eqs. (61)-(62), differs from the space charge given by the $\rho_e = c_+ = e^{-\varphi}$ [Eq. (27)]. At high selectivity, only the counterion contributes to the space charge density, while under the DH approximation, the coion also contributes – [this is the factor 2 in Eq. (62)]. If the space charge density is different, so is the driving force for the velocity. As a result, the velocity given by Eq.(63) differs from that given by Eq. (32). Naturally, the form of the advective current changes as well – see Ref. [58]. Hence, Manghi et al. [57] extension of the advective current, given by Eq. (57), from low to high concentrations is incorrect. Nonetheless, while it appears that their extension to high concentrations is incorrect, it appears that their Eq. (19), when evaluated for low concentrations, is similar to our expression for their conduction. That it is similar but not identical can be attributed to their interpolating function. Also, their analysis and results differ from the one given in this work. This will be discussed further.

III. SURFACE CHARGE REGULATION

In our derivation thus far, the surface charge density has been assumed to be a spatial constant that does not change as the environment around it changes. In the remainder, we will continue with the assumption of spatial independence, but we will alleviate the assumption that the surface charge does not vary with the environment.

The pioneering work of Stein et al. [50] showed that when the surface charge is spatially constant, one finds that the conductance depends on the surface charge and is concentration-independent at low concentrations[Eq. (5)]. Stein et al. [50] also showed that the surface charge density could be modulated by varying the *p*H. Nonetheless, while the value of the conductance changed, the slope of the conductance did not appear to change. The fact that the slope did not change was later verified by Schoch et al. [69,70] and very recently by Wang et al. [71].

However, Smeets et al. [72] showed that under certain conditions, the conductance exhibited a non-zero slope. This change in slope was attributed to a concentration dependency of the surface charge density.

In recent years, it has been suggested that the surface charge density, σ_s, is regulated through the Langmuir isotherm [54–56,58], and that it depends on the potential at the surface, $\varphi_s = \varphi(r=1)$,

$$\sigma_s = \frac{\tilde{\sigma}_s}{\tilde{\sigma}_d} = \frac{\tilde{F}\tilde{n}}{\tilde{N}_a\tilde{\sigma}_d}\left[1+10^{\mathrm{pK}-\mathrm{pH}_\infty}\exp\left(-\frac{\tilde{\varphi}_s}{\tilde{\varphi}_{th}}\right)\right]^{-1}. \quad (64)$$

Here, $\tilde{N}_a$ is Avogadro's constant, $\tilde{n}$ is the maximal number of ionizable sites per unit area, $p\mathrm{K}$ is the disassociation constant, and $p\mathrm{H}_\infty$ is the $p\mathrm{H}$ in the bulk concentration. Using the Langmuir isotherm, various models have predicted have various slopes. In particular, it has been observed that, without convection, the slope of the conductance-concentration plot, α, takes the specific values of $\frac{1}{3}$ [54] and $\frac{1}{2}$ [55]. Recently, using numerical simulations, Uematsu et al. [56] demonstrated that the slope transitions continuously between 0 to $\frac{1}{2}$.

Nonetheless, while the findings of Uematsu et al. [56] can numerically explain the various slopes observed in experiments, the theoretical understanding of the underlying physics is still missing. Also, the framework of surface charge regulation alone is unable to predict slopes larger than $\frac{1}{2}$. For example, Noy and coworkers [3,73] have measured slopes ranging from $\frac{1}{2}$ to 1 in their system of carbon nanotubes porins. Green et al. [67,68] measured a slope of 1 in their silicon-based channels. In their recent work, Noh and Aluru [74] compiled the slopes of many nanofluidic systems and showed that the slopes vary continuously from 0 to 1. As such, there is a non-trivial knowledge gap regarding slopes that are larger than $\frac{1}{2}$. The case of slopes

405 that are smaller than $\frac{1}{2}$ are considered first and the case of slopes exceeding $\frac{1}{2}$ will be addressed
406 further below.

407 Here, we leverage the derivations of Sec. II.C to recapitulate the results of Uematsu et
408 al. [56] in an almost analytical manner (i.e., $\alpha \in [0, \frac{1}{2}]$). In the next section, we will extend our
409 solution to account for convection and show that α can take *any* value between 0 and 1. In the
410 Discussion (Sec. V), we will discuss another mechanism related to entrance effects, that
411 changes the slope to 1.

412 From Eq. (26) we find the surface potential $[\varphi_s = \varphi(r=1)]$

413 $$\tilde{\varphi}_s / \tilde{\varphi}_{th} = -\ln[\varepsilon^2 \sigma_s (\sigma_s - 4)]. \tag{65}$$

414 Once more, $\sigma_s = \tilde{\sigma}_s / \tilde{\sigma}_d$ is the non-dimensional surface charge density. Substitution of Eq.
415 (65) into Eq. (64) yields a third-order polynomial that determines the surface charge density

416 $$\sigma_s^3 - 4\sigma_s^2 + (\beta\varepsilon^2)^{-1}\sigma_s + (\beta\varepsilon^2)^{-1}\gamma = 0, \tag{66}$$

417 where

418 $$\beta = 10^{\mathrm{pK}-\mathrm{pH}_\infty}, \tag{67}$$

419 $$\gamma = \tilde{F}\tilde{n} / (\tilde{N}_a \tilde{\sigma}_d). \tag{68}$$

420 It can be observed from Eq. (66) that the surface density, σ_s, depends on three parameters:
421 $\gamma, \beta, \varepsilon$. This contrasts with the dimensional form of Eq. (66), which depends on five
422 parameters [56]: $\mathrm{pK}, \mathrm{pH}_\infty, c_0, n, a$. In fact, the number of parameters in Eq. (66) can be reduced
423 to two: $\gamma, \beta\varepsilon^2$. This reduction to a more general equation will not only provide us with more
424 robust results but will also allow us to better interpret the numerical results of Uematsu et
425 al. [56] (Sec. IV).

426 Equation (66) can be solved analytically with any symbolic math program. Surprisingly,
427 the solution for a third-order polynomial that depends only on two parameters is not tractable.

Thus, we do not present the long solution here. Instead, we show that three solutions are immediately recovered. For the case that $\beta\varepsilon^2 \ll 1$, the σ_s^2 and σ_s^3 are negligible. This leads to the concentration-independent solution

$$\sigma_{s,0} = -\gamma\,, \tag{69}$$

For the case that $\beta\varepsilon^2 \gg 1$ the linear term is negligible. This leads to two solutions for large and intermediate surface charges, respectively [58]

$$\sigma_{s,\frac{1}{3}} = -[\gamma/(\beta\varepsilon^2)]^{1/3}\,, \tag{70}$$

$$\sigma_{s,\frac{1}{2}} = -\tfrac{1}{2}[\gamma/(\beta\varepsilon^2)]^{1/2}\,. \tag{71}$$

Section IV utilizes the dimensional form of these equations

$$\tilde{\sigma}_{s,0} = -\gamma\tilde{\sigma}_d = -\tilde{F}\tilde{n}/\tilde{N}_a\,, \tag{72}$$

$$\tilde{\sigma}_{s,\frac{1}{3}} = -[\gamma/(\beta\varepsilon^2)]^{1/3}\tilde{\sigma}_d = -(2\tilde{\varepsilon}_0\varepsilon_r\tilde{R}_g\tilde{T}z\tilde{c}_0\gamma/\beta)^{1/3}\,, \tag{73}$$

$$\tilde{\sigma}_{s,\frac{1}{2}} = -\tfrac{1}{2}[\gamma/(\beta\varepsilon^2)]^{1/2}\tilde{\sigma}_d = -(\tfrac{1}{2}\tilde{a}\tilde{F}\tilde{c}_0 z\gamma/\beta)^{1/2}\,. \tag{74}$$

Equation (74) is identical to the equation suggested by Ref. [55], while Eq. (73) is identical to the equation suggested by Ref. [54]. It should also be mentioned that in both works, these equations were derived using the cross-sectional average of the electric-potential distribution. In contrast to Refs. [54,55], here we have derived these two relations from local considerations. In the next section, we will demonstrate that the insertion of Eqs. (72)-(74) in Eq. (2) will yield conductance slopes of 0 [56]to $\frac{1}{3}$ [54,56] to $\frac{1}{2}$ [55,56]. Since Refs. [54–56] conducted a comparison with experiments; we will not undertake a similar comparison. Instead, our purpose thus far has been to demonstrate that these three different models are derived from the same universal equation [Eq. (66)] representing the same theory. In the next section, we confirm Uematsu et al. [53] finding that the slope can vary smoothly from 0 to $\frac{1}{2}$.

In their work, Manghi et al. [57] considered the case that the unity term in Eq. (64) is negligible relative to the pH term. Indeed, in the limit of high surface charges, this is the case. However, if one neglects this term before inserting Eq. (65) into Eq. (64), then one changes the resulting governing equation for the surface charge density [Eq. (66)]. As a result, the linear σ_s contribution is removed, and the slope varies between the two limiting solutions of $\frac{1}{3}$ to $\frac{1}{2}$. Manghi et al. [57] indeed only consider the two specific cases of $\alpha=\frac{1}{3}$ and $\alpha=\frac{1}{2}$ which they term "high surface charge density (inhomogeneous) GCE" and "low surface charge density (homogeneous) GCE" limits, respectively. Once more, it appears that in these two distinct limits, their approximations are correct. However, they don't show the gradual and smooth transition from $\alpha=\frac{1}{3}$ (or $\alpha=0$) to $\alpha=\frac{1}{2}$. While potentially they could have predicted the doubling presented in this work, it appears that they only considered for the particular cases of $\alpha=\frac{1}{3}$ and $\alpha=\frac{1}{2}$ [additional comments regarding the $\alpha=\frac{1}{2}$ scenario described in Manghi et al. [57] – their Eq. (24) – can be found below Eq. (79)], and they overlooked the general solution.

IV. CONDUCTANCE

This section is divided into three. First, we discuss the behavior of the Ohmic conductance (i.e., the effects of convection to the conductance are negligible) (Sec. IV.A). Second, we discuss the contribution of convection without slip to the conductance (Sec. IV.B). Finally, we discuss the contribution of convection with slip to the conductance (Sec. IV.C). In all three sub-sections, we consider the effect of surface charge regulation [Eqs. (72)-(74)].

Before proceeding with the analysis, it should be noted that while this analysis focuses on the electrical conductance, one can also consider the mass transport coefficients. This is the transport coefficient matrix that relates the volume flux and electrical current densities to the

pressure drop and electric field. It can be shown that such a matrix satisfies Onsager reciprocity. An analysis of this matrix (without the effects of slip) was conducted in our previous work [58].

A. Convection-less conductance

Consider the low concentration response of the Ohmic conductance – this is the limit when the concentration term in Eq. (2) is negligible ($\tilde{N} \gg \tilde{c}_0$)

$$\tilde{G}_{Ohmic,low} = \frac{2\pi\tilde{a}}{\tilde{L}} \frac{z\tilde{F}\tilde{D}}{\tilde{R}_g\tilde{T}} \left|\tilde{\sigma}_s\right| . \tag{75}$$

This expression was derived in Sec. II.F [Eq. (56)] but is also recapitulated by inserting Eq. (36) into Eq. (5). Observe that Eq. (75) is explicitly concentration-independent, yet there is an implicit dependency on the concentration through the surface charge. In Eqs. (72)-(74) we saw that $\tilde{\sigma}_s \sim \tilde{c}_0^{\alpha}$. This leads to $\tilde{G}_{ohmic} \sim \tilde{c}_0^{\alpha}$. Hence, *the conductance is implicitly dependent on the concentration, and the slope of the Ohmic conductance is the same slope of the surface charge density,* α .

Under the assumption of negligible convection, we can use Eq. (2) in the entire concentration domain. We insert into it Eqs. (72)-(74) and plot the conductance for these three specific cases (**Figure 4**). At high concentrations, when the effects of the surface charge are negligible, these three lines collapse on each other, and the slope is 1. At low concentrations, however, the behavior of the three curves varies drastically, where it becomes evident that the slope has a dependence on the concentration (via surface charge regulation). Our theoretical predictions are verified by direct numerical simulations of the PNP equations (Appendix B) – the correspondence between theory and simulation is remarkable.

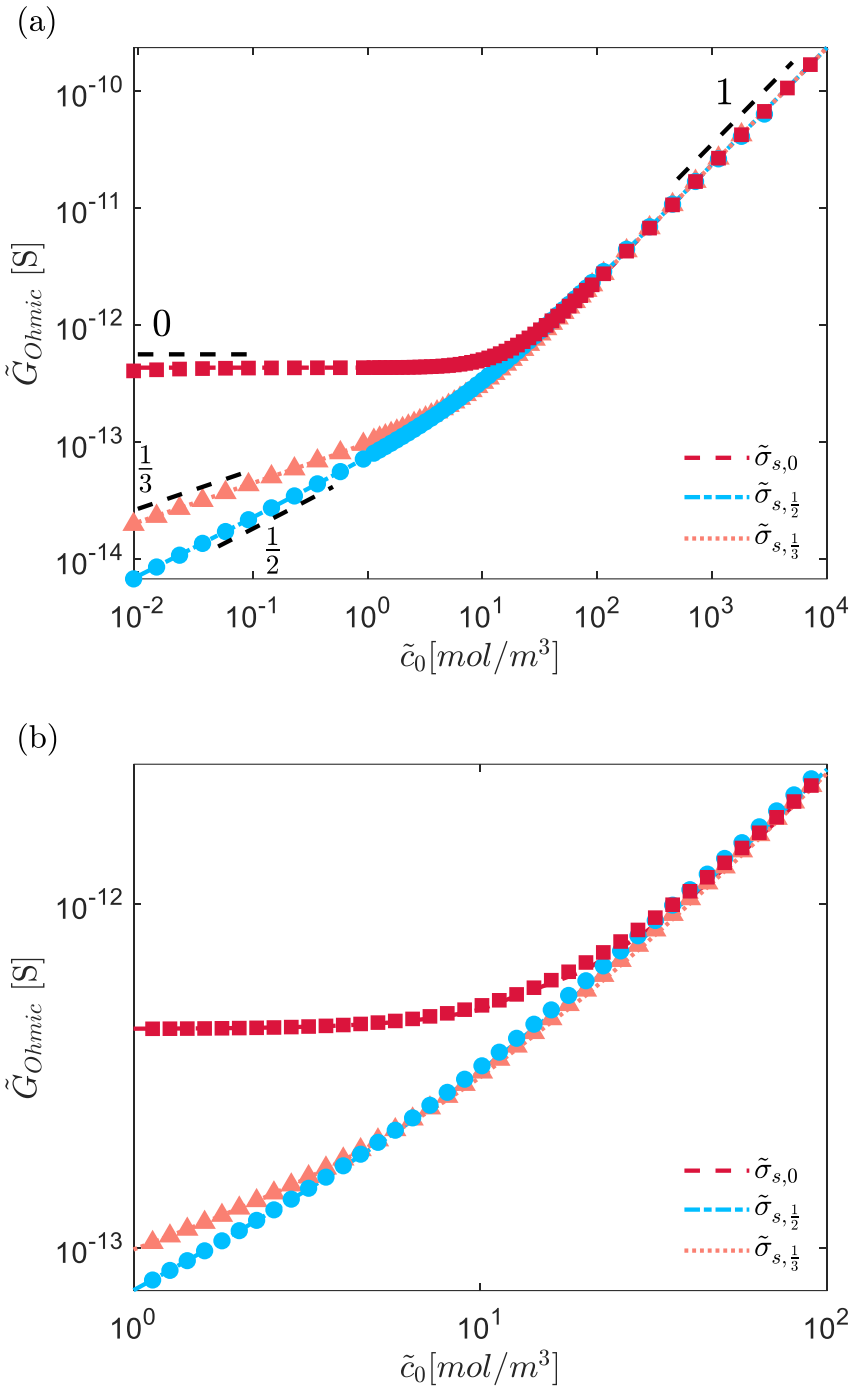

Figure 4. (a) Ohmic conductance versus concentration [Eq. (2)] for the three surface charge densities: $\tilde{\sigma}_{s,0}$, $\tilde{\sigma}_{s,\frac{1}{3}}$, $\tilde{\sigma}_{s,\frac{1}{2}}$ [Eqs. (72)-(74), respectively]. Theory is denoted by lines, and simulations are denoted by markers. (b) A zoomed-up view of (a). The values for the simulations are given in **Table 1** and **Table 2**.

While the purpose of the numerical simulations was to verify our analytical results, the technical feat of these simulations is also noteworthy– namely, the high resolution of these simulations. In most state-of-the-art 2D or 3D simulations, the typical concentration range

covers only three decades with 2-4 points per decade. Here, we investigate the changes over six decades of concentrations. We have 5 points per decade of concentration in regions when the slope is not transitioning from one value to another and 20 points per decade of concentration in regions where the slope is transitioning. In fact, in **Figure 4**(b), it is challenging to differentiate the curve from the almost continuous array of markers representing the numerical simulations due to the high density of points.

Figure 4 considers only three particular solutions of Eq. (66) with slopes of 0, $\frac{1}{3}$ and $\frac{1}{2}$. We will now demonstrate that the slope varies continuously between 0 to $\frac{1}{2}$. To that end, we review the numerical approach of Uematsu et al. [56], whose approach will be used here as well, albeit we supplement it with a more theoretical approach.

Uematsu et al. [56] numerically solved the 1D PNP equations and investigated how the slope of the conductance varied with the $(\mathrm{pK}, \mathrm{pH}_\infty, \tilde{c}_0, \tilde{n}, \tilde{a})$ phase space of the Langmuir isotherm [Eq. (64)]. In their simulations, they set $\tilde{a}, \tilde{n}, p\mathrm{K}$ to several particular values and investigated the effects of pH_∞ and $\tilde{c}_0$. Since they utilized numerical simulations, they considered both low and high concentrations. Expectedly at high concentrations, they showed that the slope was 1 (**Figure 4**, which will not be considered in our upcoming analysis). At low concentrations, Uematsu et al. [56] showed that the slope α varies from 0 to $\frac{1}{2}$. To that end, they numerically calculated the conductance for each configuration in their $\tilde{c}_0 - \mathrm{pH}$ phase space, and they evaluated the slope via

$$\alpha = \frac{d(\ln \tilde{G})}{d(\ln \tilde{c}_0)}. \tag{76}$$

Thereafter, they plotted a 2D color plot of the value of α for the $\tilde{c}_0 - \mathrm{pH}$ phase space.

Here, we recapitulate the low-concentration results of Uematsu et al.'s Figure 1 [56] – this is our **Figure 5**, albeit our approach is different. First, our analytical derivation is limited to

low concentration. However, the variation with α occurs only at low concentrations. Second, our approach is almost entirely analytical. The only numerical evaluation used here is in solving Eq. (66) , which was analytically derived. Specifically, we use the Newton-Raphson method to solve Eq. (66) for $\tilde{\sigma}_s$. Third, Uematsu et al. [56] have five parameters. Our approach has two parameters: γ and $\beta\varepsilon^2$. Upon solving Eq. (66), the surface charge density, $\tilde{\sigma}_s$ is inserted into $\tilde{G}_{Ohmic,low}$ [Eq.(75)]. We evaluate the slope using Eq. (76). The benefits of our approach are two-fold: technical and physical insights.

On the technical side, Uematsu et al.'s [56] results were based on direct numerical simulations of the PNP equations. Even though 1D simulations are no longer computationally costly, scanning a 5D phase space can be burdensome. Even scanning a 2D phase space $(\tilde{c}_0 - \mathrm{pH})$ takes time, and the final results of Eq. (76) eventually depend on the resolution of the phase space. For example, Figure 1 of Ref. [56] is pixilated. In contrast, our approach is by far less computationally demanding. Our approach allows us to scan the phase space to any desired resolution in an almost instantaneous manner. As a result, **Figure 5** is not pixelated.

Figure 5 also provides new physical insights into the conductance at low concentrations. Figure 1 of Uematsu et al.'s [56] exhibited several stripes of the same color (that denote constant slopes). The origin of these stripes was not explained. Our theoretical approach provides a remarkable and intuitive explanation – these are lines of constant $\beta\varepsilon^2$ [this result can be recovered by taking $\log_{10}(\beta\varepsilon^2)$ and inserting Eqs. (11) and (67)]. In our two-parameter approach $(\gamma, \beta\varepsilon^2)$, which follows the five-parameter approach of Uematsu et al.'s [56], we set γ and scan $\beta\varepsilon^2$. Hence, values of constant $\beta\varepsilon^2$ should lead to values of constant slope. In, the $\tilde{c}_0 - \mathrm{pH}$ plane there are stripes. **Figure 5** demonstrates two key results: 1) the slope varies continuously between 0 to $\frac{1}{2}$; 2) the slopes are lines of constant $\beta\varepsilon^2$.

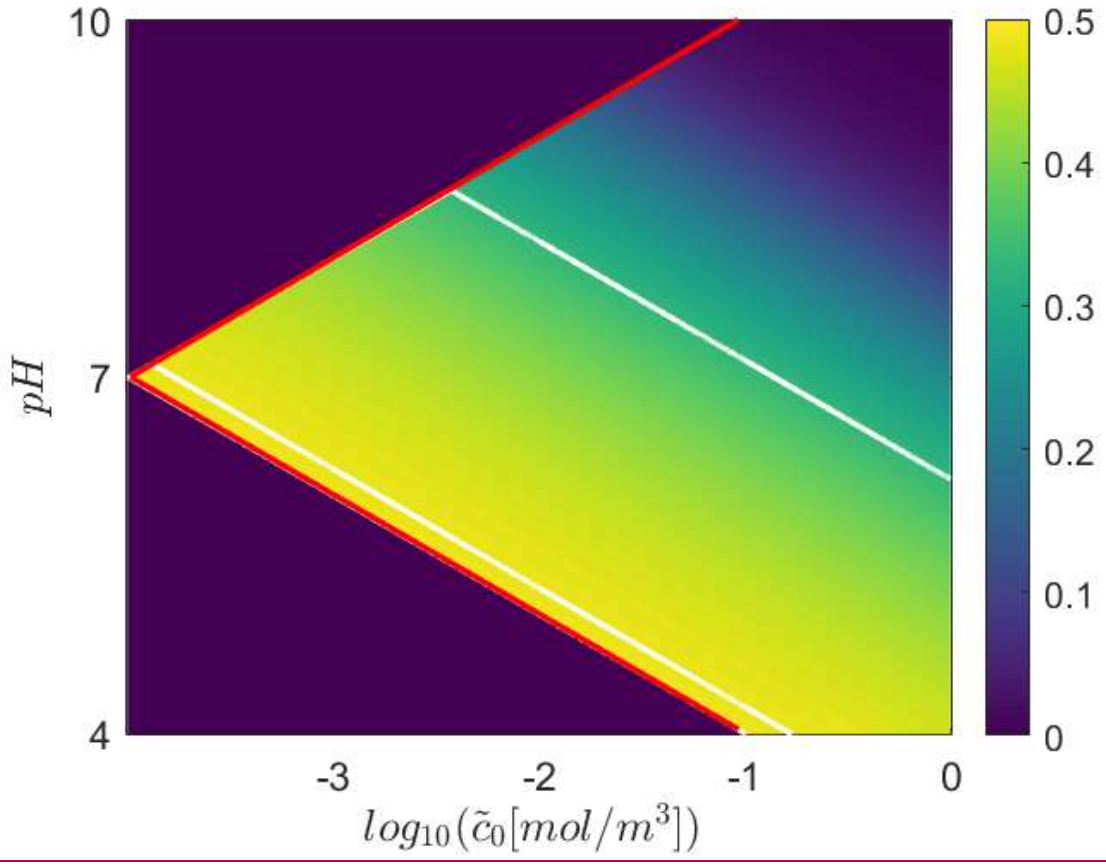

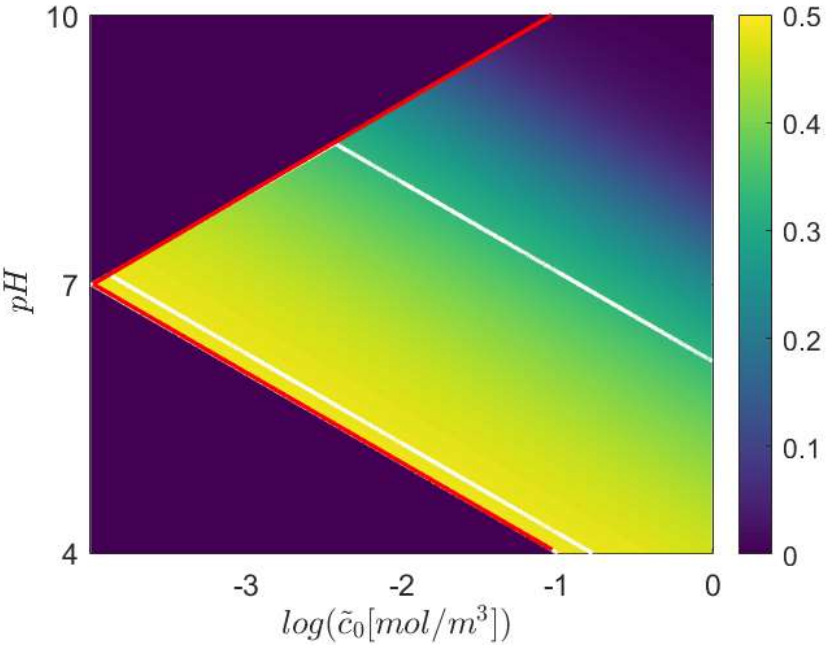

Figure 5. Color map of the slope α, in the $\tilde{c}_0 - \mathrm{pH}$ plane of the Ohmic conductance, $\tilde{G}_{Ohmic,low}$ [Eq. (75)]. White diagonal lines denote the lines of constant

slope of $\alpha = \frac{1}{3}$ and $\alpha = 0.483$. The thick red lines denote cutoffs discussed in the main text. Here we used the values of Figure 1 from Uematsu et al. [56]: $\tilde{a} = 35[\text{nm}]$, pK=5, and $\tilde{n} = 0.2[\text{nm}^{-2}]$.

Further below, we discuss the thick red lines at the top and bottom of the phase space of **Figure 5**. These lines are the cutoffs, as suggested by Ref. [56], when the contribution of H_+ ions to the conductance is no longer non-negligible.

B. Convection without slip

Before we present the results pertaining to the effects of convection, we wish to make three general statements. 1) It is intuitive and elementary that convection should increase the conductance. 2) It is not intuitive whether or not convection should vary the slope of the conductance. 3) Nor is it intuitive whether or not the effects of the slip length will vary the slope. We will shortly show that no-slip convection increases the conductance but doesn't change the slope α. Inclusion of slip changes further increases the conductance and varies the slope from α to 2α.

Consider the conductance that accounts for the Ohmic contribution and the no-slip advective term

$$\tilde{G}_{total,no-slip} = \tilde{G}_{Ohmic,low} + \tilde{G}_{adv,no-slip}. \tag{77}$$

We return to Eq. (57)

$$\tilde{G}_{adv,no-slip} = -8\tilde{\kappa}_{cond}\varepsilon^2 \text{Pe}\left[\frac{\tilde{\sigma}_s}{\tilde{\sigma}_d} + 4\ln\left(1 - \frac{1}{4}\frac{\tilde{\sigma}_s}{\tilde{\sigma}_d}\right)\right]\frac{\pi\tilde{a}^2}{\tilde{L}}. \tag{78}$$

Since $\tilde{\kappa}_{cond}\varepsilon^2$ is concentration-independent [Eq. (60)] then $\tilde{G}_{adv,no-slip}$ is also explicitly concentration-independent. However, $\tilde{G}_{adv,no-slip}$ implicitly depends on the concentration through the surface charge density.

We will now consider two situations $\sigma_s = \tilde{\sigma}_s / \tilde{\sigma}_d \ll 1$ and $\sigma_s \gg 1$. The case of small surface charge yields

$$\tilde{G}^{(\tilde{\sigma}_s/\tilde{\sigma}_d \ll 1)}_{adv,no-slip} = \tilde{\kappa}_{cond} \varepsilon^2 \mathrm{Pe} \frac{\pi \tilde{a}^2}{\tilde{L}} \left(\frac{\tilde{\sigma}_s}{\tilde{\sigma}_d} \right)^2 . \tag{79}$$

This contribution was previously derived in Refs. [55,57]. This solution corresponds to the solution predicted by the uniform potential model [75] (see Ref. [58] for a discussion regarding the limitations of the uniform potential model for nanopores with $\varepsilon \gg 1$). Eq. (79) predicts a σ_s^2 scaling while $\tilde{G}_{Ohmic,low}$ predicts a linear scaling. Hence, one might expect a change in the slope. Yet, in the limit $\sigma_s \ll 1$ one has $\tilde{G}_{total,no-slip} \sim \tilde{G}_{Ohmic,low} \sim \tilde{c}_0^{\alpha}$. Hence, there is no change in slope. Manghi et al. [57] also derived Eq. (79) in their work, only for the particular slope $\alpha = \frac{1}{2}$, and they state (in the notation of this work), "At low but intermediate $\tilde{c}_0$ and high enough slip length the second term may dominate and lead to a cross-over exponent of 1." Such a statement is not entirely correct. In order for $\left| \bar{G}_{adv,slip} / \bar{G}_{Ohmic} \right| \sim O(1)$, once must have $\left| \mathrm{Pe} b \sigma_s \right| \sim O(1)$ which requires that $b \sim O(\sigma_s^{-1}) \gg 1$. However, in order for $\left| \bar{G}_{adv,slip} / \bar{G}_{Ohmic} \right| \gg 1$ one must require that $b \ggg 1$. As we will discuss in the Discussion, the slip-length is a material property that cannot be increased without limit. Further, we will shortly show that once one takes the $\sigma_s \gg 1$ limit combined with the slip length, a value of $b \sim O(1)$ predicts the doubling of the slope.

For large surface charges, $\sigma_s \gg 1$, which is the typical case for highly selective nanochannels, the logarithmic term in Eq. (78) is negligible. This results in

$$\tilde{G}^{(\tilde{\sigma}_s/\tilde{\sigma}_d \gg 1)}_{adv,no-slip} = -8 \tilde{\kappa}_{cond} \varepsilon^2 \mathrm{Pe} \frac{\pi \tilde{a}^2}{\tilde{L}} \frac{\tilde{\sigma}_s}{\tilde{\sigma}_d} . \tag{80}$$

Inserting Eqs. (56) and (80) into Eq. (77) yields

$$\tilde{G}_{total,no-slip}^{(\tilde{\sigma}_s/\tilde{\sigma}_d \gg 1)} = -4\tilde{\kappa}_{cond}\varepsilon^2 \frac{\tilde{\sigma}_s}{\tilde{\sigma}_d}\frac{\pi\tilde{a}^2}{\tilde{L}}(1+2\mathrm{Pe})\,. \tag{81}$$

Indeed, the convection term substantially increases the conductance [60]. For example, for a KCl water-based electrolyte at room temperature, one finds that the Peclet number [Eq. (13)] is approximately 0.45 such that convection increases the conductance by approximately 100%. However, Eq. (81) predicts that the slope of the conductance remains unchanged relative to the Ohmic conductance (i.e., $\tilde{G}_{total,no-slip} \sim \tilde{\sigma}_s \sim \tilde{c}_0^{\alpha}$). Note that in our calculations, we use the complete form of Eq. (57) [or Eq. (78)] whereby the analysis leading up to Eq. (81) has been used for demonstration purposes to understand each of the contributions better.

Figure 6(a)-(c) compares the theoretical predictions of Eq. (77) to numerical simulations for the three cases of (a) $\tilde{\sigma}_{s,0}$, (b) $\tilde{\sigma}_{s,\frac{1}{3}}$, (c) $\tilde{\sigma}_{s,\frac{1}{2}}$ The solid red lines are the Ohmic conductance previously shown in **Figure 4**. For presentation purposes, we have not included the convection-less simulations $(\mathrm{Pe}=0)$ that were shown in **Figure 4**. The dashed blue lines in each of the plots represent the case of $\mathrm{Pe}=0.45$ with a no-slip boundary condition $(b=0)$. The excellent correspondence confirms in all three cases confirms the prediction that no-slip convection increases the conductance but does not change the slope.

(a)

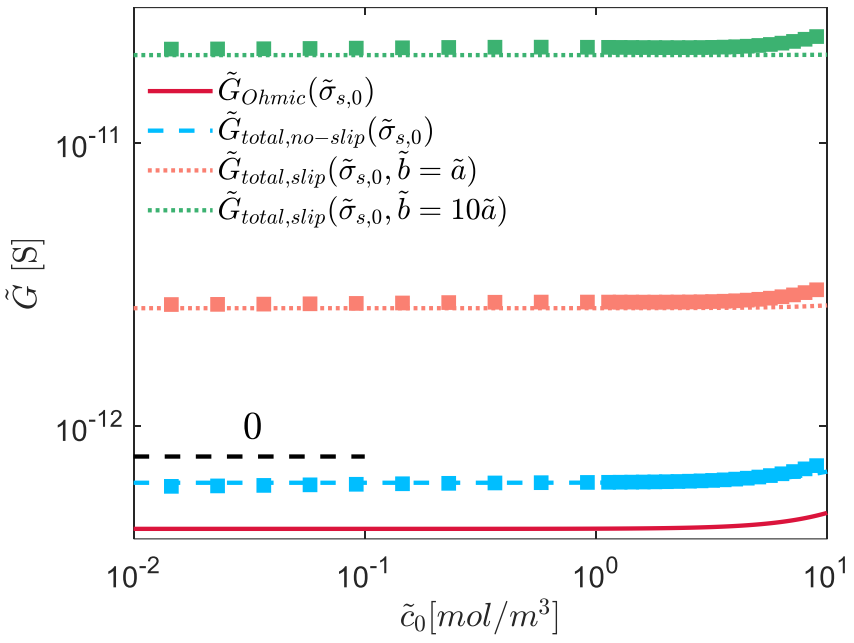
$\tilde{G}_{Ohmic}(\tilde{\sigma}_{s,0})$
$\tilde{G}_{total,no-slip}(\tilde{\sigma}_{s,0})$
$\tilde{G}_{total,slip}(\tilde{\sigma}_{s,0}, \tilde{b} = \tilde{a})$
$\tilde{G}_{total,slip}(\tilde{\sigma}_{s,0}, \tilde{b} = 10\tilde{a})$
10^{-11}
10^{-12}
0
$\tilde{G}$ [S]
10^{-2}
10^{-1}
10^{0}
10^{1}
$\tilde{c}_0[mol/m^3]$

610

(b)

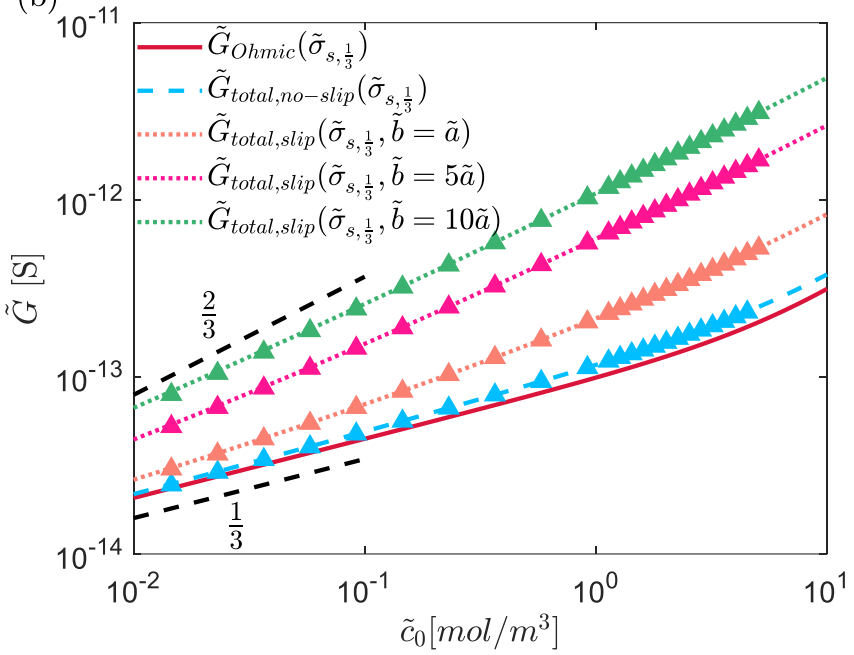
$\tilde{G}_{Ohmic}(\tilde{\sigma}_{s,\frac{1}{3}})$
$\tilde{G}_{total,no-slip}(\tilde{\sigma}_{s,\frac{1}{3}})$
$\tilde{G}_{total,slip}(\tilde{\sigma}_{s,\frac{1}{3}}, \tilde{b} = \tilde{a})$
$\tilde{G}_{total,slip}(\tilde{\sigma}_{s,\frac{1}{3}}, \tilde{b} = 5\tilde{a})$
$\tilde{G}_{total,slip}(\tilde{\sigma}_{s,\frac{1}{3}}, \tilde{b} = 10\tilde{a})$
10^{-11}
10^{-12}
10^{-13}
10^{-14}
$\frac{2}{3}$
$\frac{1}{3}$
$\tilde{G}$ [S]
10^{-2}
10^{-1}
10^{0}
10^{1}
$\tilde{c}_0[mol/m^3]$

611

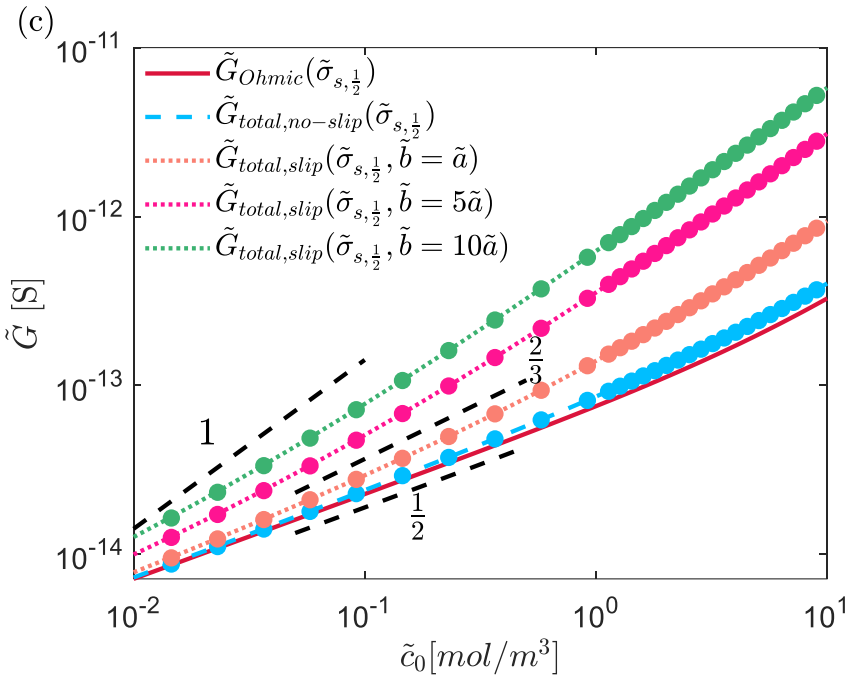

Figure 6. Conductance-concentrations curves predicted by Eq. (83) for (a) $\tilde{\sigma}_{s,0}$ [Eqs. (72)], (b) $\tilde{\sigma}_{s,\frac{1}{3}}$ [Eqs. (73)], (c) $\tilde{\sigma}_{s,\frac{1}{2}}$[Eq. (74)]. Theory is denoted by lines, and simulations are denoted by markers. The values for the simulations are given in **Table 1** and **Table 2**.

C. Convection with slip

We return to Eq. (58) , which gives the expression for the contribution of the slip length to the conductance

$$\tilde{G}_{adv,slip} = 4\tilde{\kappa}_{cond}\varepsilon^2 \mathrm{Pe}\left(\frac{\tilde{\sigma}_s}{\tilde{\sigma}_d}\right)^2 \frac{\tilde{b}}{\tilde{a}}\frac{\pi\tilde{a}^2}{\tilde{L}}. \tag{82}$$

Note that while this term depends on the area $\pi\tilde{a}^2$, the slip length is divided by the radius such that the term is linear with the radius. This is expected of a phenomenon that originates at a surface. Similarly, the low concentration Ohmic conductance [Eq. (56)] scales with the perimeter. We add Eq. (82) to Eq. (77) to get an expression for the conductance that accounts for all three contributions

$$\tilde{G}_{total,slip} = \tilde{G}_{total,no-slip} + \tilde{G}_{adv,slip} = \tilde{G}_{Ohmic,low} + \tilde{G}_{adv,no-slip} + \tilde{G}_{adv,slip}. \tag{83}$$

628 Two observations are noteworthy. First, as can be expected, $\tilde{G}_{adv,slip}$ further increases the
629 conductance. Second, $\tilde{G}_{adv,slip}$ scales quadratically with the surface charge, $\tilde{G}_{adv,slip} \sim \tilde{\sigma}_s^2 \sim \tilde{c}_0^{2\alpha}$.
630 As a result, the overall slope of $\tilde{G}_{total,slip}$ changes relative to that of $\tilde{G}_{total,no-slip}$. If $\tilde{G}_{total,no-slip}$ has
631 a slope $\alpha \in [0, \frac{1}{2}]$ then $\tilde{G}_{total,slip}$ has a slope $2\alpha \in [0,1]$. We demonstrate this change of slope in
632 two different manners.

633 The dotted orange, magenta, and green lines of **Figure 6**(a)-(c) compare the theoretical
634 predictions of Eq. (83) to numerical simulations that account for convection with a non-zero
635 slip length $(b \neq 0)$. **Figure 6**(a) shows that when $\tilde{\sigma}_{s,0} \sim \tilde{c}_0^0$ [i.e. $\alpha = 0$, Eq. (72)], the slope
636 always remains $\alpha = 0$. **Figure 6**(b) shows that when $\tilde{\sigma}_{s,\frac{1}{3}} \sim \tilde{c}_0^{1/3}$ [Eq. (73)], the slope transitions
637 from $\alpha = \frac{1}{3}$ to $\alpha = \frac{2}{3}$ as the slip length is increased. **Figure 6**(c) shows that when $\tilde{\sigma}_{s,\frac{1}{2}} \sim \tilde{c}_0^{1/2}$
638 [Eq. (74)], the slope transitions from $\alpha = \frac{1}{2}$ to $\alpha = 1$ as the slip length is increased. The
639 correspondence between simulations and theory is excellent and demonstrates the dependency
640 of the conductance on $\tilde{\sigma}_s$ and $\tilde{b}$.

641 Several comments are warranted. The $\frac{2}{3}$ slope was recently measured in an experimental
642 work that utilized carbon nanotube porins [73]. These experimental results [73] correspond
643 well to the theoretical predictions of Ref. [57] who predicted a slope of $\alpha = \frac{2}{3}$ (due to the
644 effects of slip). However, Ref. [57] specifically considered $\tilde{\sigma}_{s,\frac{1}{3}} \sim \tilde{c}_0^{1/3}$ (i.e. $\tilde{G}_{total,slip} \sim \tilde{c}_0^{2/3}$) and
645 overlooked the more general $\tilde{G}_{total,slip} \sim \tilde{c}_0^{2\alpha}$ solution that holds for all $\alpha \in [0, \frac{1}{2}]$. One of the
646 main findings of this work is the generality of the transition from a slope of α (for convection
647 without slip) to 2α (for convection with slip). The slope of 1 corresponds to the experimental
648 finding of Ref. [3].

649 It can be argued that the slope in **Figure 6**(c) does not truly reach a slope of 1. Below we
650 discuss how decreasing the concentrations or increasing the slip lengths would show the slope
651 indeed reaches 1. Beforehand, for demonstration purposes, we use the "unrealistic" case
652 $\tilde{b} = 100\tilde{a}$ to show that the slope indeed varies from 0 to 1. We use the parameter set $(\tilde{a}, \tilde{n}, p\mathrm{K})$
653 used to calculate for **Figure 5**. We use the same parameter set but rather than inserting it into
654 the Ohmic contribution [Eq. (75)], we insert the calculated value of σ_s in the equation that
655 accounts for convection and slip [Eq. (83)]. The results are shown in **Figure 7**, where it is
656 observed that $\alpha \in [0,1]$.

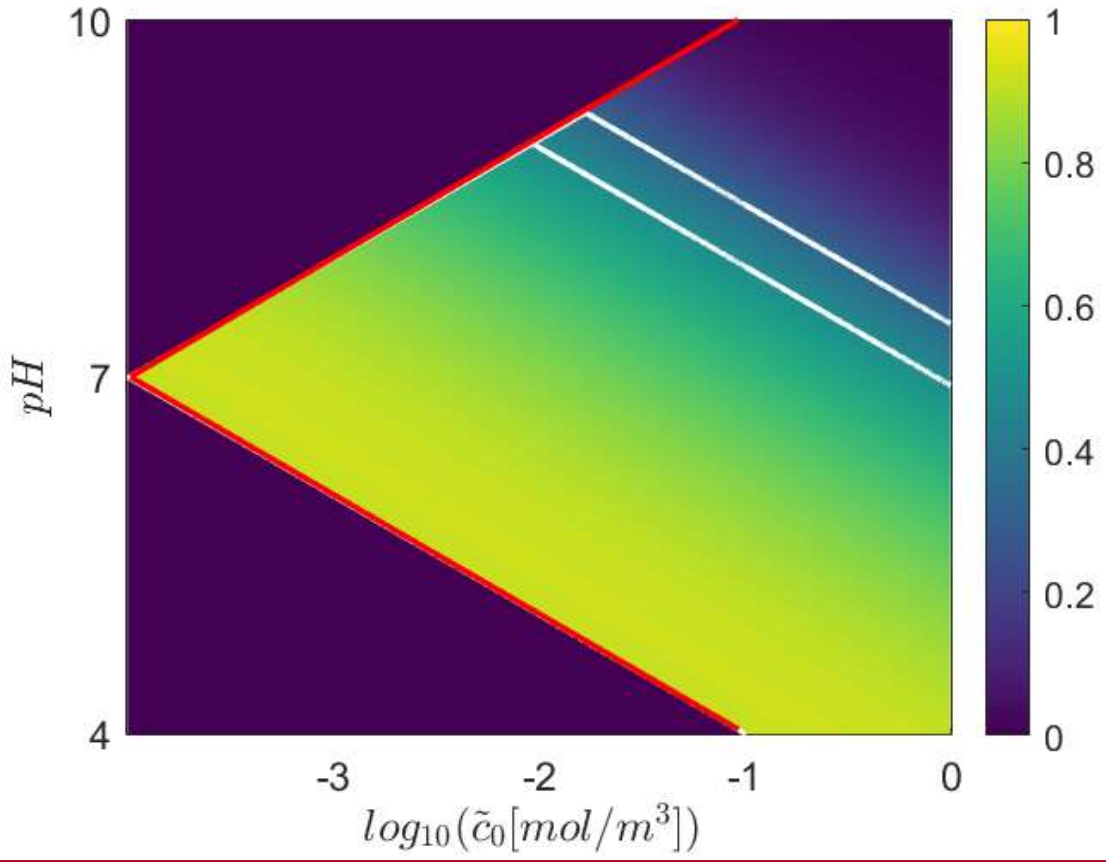

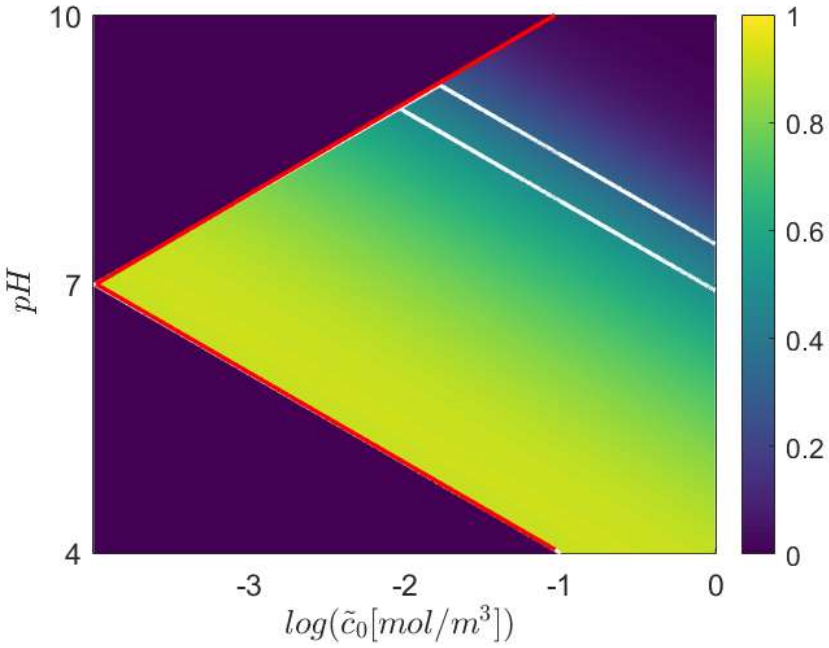

Figure 7. Color map of the slope, α, in the $\tilde{c}_0 - \text{pH}$ plane for $\tilde{G}_{total,slip}$ [Eq. (83)]. The white diagonal lines denote the lines of constant slope of $\alpha = \frac{1}{3}$ and $\alpha = 0.483$ shown in **Figure 5**.

To achieve a slope of 1, one can either consider smaller $\tilde{c}_0$ or larger $\tilde{b}$. In both cases, this will result in $\tilde{G}_{adv,slip}$ dominating $\tilde{G}_{total,slip}$. However, while both approaches are mathematically allowed, two experimental facts should be remembered. Varying the slip-length without end suffers a substantial setback – the slip length is a material property that cannot be tuned as desired. Several comments are noteworthy. First, A number of works have shown that the slip length can take values $\tilde{b} = 50 - 200\text{nm}$ [76–79]. If the slip length is indeed a material property, then a CNT channel with a radius of $\tilde{a} = 10\text{nm}$ would have a dimensionless slip length of $b = 5 - 20$ which is only five times smaller than that used in **Figure 7** but well within the values used in **Figure 6**. Second, it has been recently suggested [80], through statistical physics considerations and molecular dynamics simulations, that the slip length can be varied by changing a few fluid-structure interaction parameters. However, these parameters are also characteristics of the material and hence from our perspective, indeed, $\tilde{b}$ is a non-tunable property. Third, in a recent work that utilized molecular dynamic simulations, it was shown that for pores with large aspect ratios $(L \gg a)$, the slip length appears to be a property of the material. However, for $L \geq a$, the slip length appears to have a certain enhancement. In this work, we have utilized the assumption of $L \gg a$ which is realistic to the scenario for CNTs and BNNT. Nonetheless, future works should consider how the conductance in short pores, $L \sim a$, varies with slip.

In Sec. II.A. we assumed that the contributions of hydrogen and hydroxide to the conductance are negligible. However, this assumption fails at extremely low concentrations that can be probed experimentally. When this occurs, our assumption that the current is transported only by the salts no longer holds. Thus, at sufficiently low concentrations, a cutoff is needed. These are the thick red lines in **Figure 5** and **Figure 7** (as suggested by Uematsu et al. [56]). The concentrations used in this work are representative of realistic experimental

conditions. Hence, within the limits considered in this model, we have still demonstrated the slope $\tilde{G}_{total,slip}$ changes due to surface charge regulation and convection. Future works should attempt to model the case of fours species with a pore.

V. DISCUSSION AND CONCLUSIONS

This work aims to elucidate the underlying theory affecting the change of the slope of the electrical conductance at low concentrations, as numerous phenomena are added. Specifically, we start with the Ohmic conductance. We then consider surface charge regulation, convection without slip, and convection with slip. The contribution of each phenomenon is analyzed separately. Specifically, we show that the Ohmic contribution, along with surface charge regulation, can have a slope $\alpha \in [0, \frac{1}{2}]$. The addition of convection without slip does not vary the slope. However, the addition of a slip length results in a change of the slope from $\alpha \in [0, \frac{1}{2}]$ to $2\alpha \in [0,1]$. This is the main finding of this work and has broad implications for theory and experiments [81].

From the theoretical standpoint, numerous past works have derived expressions for various contributions to conductance. Each of these contributions/terms holds under different assumptions, whereby the assumptions do not necessarily overlap and/or are in conflict. Also, some of these models are based on empirical reasoning. Despite such shortcomings, it has become common practice to model the total conductance, $\tilde{G}_{total,slip}$, as a superposition of these various models. In contrast, in this work, our model is an exact solution of the PNPs equations, and all terms are entirely self-consistent with each other.

In experiments, one measures the total conductance, $\tilde{G}_{total,slip}(\tilde{c}_0)$ from which the slope, α_{meas} can be extracted. From the experimental standpoint, there remain two additional unknown parameters from Eq. (83) that need to be determined. These are the $\tilde{n}$ and $\tilde{b}$.

709 Determining these is challenging because the surface charge is a complicated function of $\tilde{n}$
710 and $\tilde{c}_0$, $\tilde{\sigma}_s(\tilde{c}_0^{\alpha},\tilde{n})$, that needs to be determined by Eq. (66). We consider a number of scenarios.
711 In all these scenarios, foreknowledge of pK, which is a material property, is needed. If not,
712 this parameter also needs to be fitted or estimated:

713 - No convection (with and without slip): If one assumes that the slope has very discrete
714 values: $\alpha = 0, \frac{1}{3}, \frac{1}{2}$, it is straightforward to extract the maximal number of ionizable
715 sites per unit area, $\tilde{n}$, from Eqs. (72)-(74). If the assumption of discrete values is
716 relaxed such that $\alpha_{meas} \in [0, \frac{1}{2}]$, one can solve Eq. (66) to find what value of $\tilde{n}$ will give
717 $\alpha_{meas} = \alpha_{theory}$.

718 - With slip ($\alpha_{meas} > \frac{1}{2}$): Surface charge regulation predicts a maximal slope of $\frac{1}{2}$ (
719 $\alpha_{theory} \in [0, \frac{1}{2}]$). Hence, slip effects are necessarily present when $\alpha_{meas} > \frac{1}{2}$. For a
720 measured slope, the theoretical slope is $\alpha_{theory} = \frac{1}{2}\alpha_{meas}$. One can solve Eq. (66) to find
721 what value of $\tilde{n}$ will give $\alpha_{meas} = \alpha_{theory}$. Thereafter, the slip length can be calculated.

722 - With slip ($\alpha_{meas} < \frac{1}{2}$): This scenario, with no existing knowledge regarding the slip
723 length, is exceptionally challenging. One can use the scenarios mentioned above as two
724 possible initial guesses. Another possibility is to conduct another round of experiments
725 with a different set of conditions (i.e., different pH) such that the slope changes. Given
726 two sets of experiments and assuming that material properties are invariant to the
727 experimental conditions, calculation of $\tilde{n}$ and $\tilde{b}$ should be possible.

728 Additional theoretical and experimental complications in extracting the slope follow from
729 the unfortunate reality that other phenomena not modeled here are, possibly, present in the
730 system. For example, recently, Noh and Aluru [74] derived a model that also predicted a slope
731 of $\alpha \in [0,1]$. In contrast to this model, Noh and Aluru [74] have assumed a non-regulated

surface density (i.e. $\tilde{\sigma}_s \sim \tilde{c}_0^0$) and negligible convection. Instead, Noh and Aluru [74] introduced a new term/expression into their model related to the newly suggested phenomena of electroneutrality breakdown [82] such that their slope, α, is a free fitting parameter and serves as a proxy for the breakdown. Such an approach contrasts with the approach taken in this work. In our work, the value of the slope depends on the material properties and is not a fitting parameter. Here, the only way to vary the slope is to tune the material properties $(\tilde{n}, \tilde{b})$. Also, electroneutrality breakdown has recently been contested [66], where it was shown that the breakdown might not be as prevalent as is thought, and unique conditions are needed for the breakdown to occur. Nonetheless, the issue of electroneutrality breakdown remains an open question.

This work has shown that the effects of surface charge regulation can result in a slope of 0 to $\frac{1}{2}$. Upon the inclusion of slip, the slope varies between 0 and 1. Yet, an additional mechanism, independent of surface charge regulation and slip, also predicts a slope of 1. This mechanism is related to the added contributions of the field-focusing resistances and microchannels resistances [67,68,83]. In many works, typically, only the nanochannel is modeled such that, naturally, only the nanochannel conductance arises. However, if one accounts for the adjacent microchannels, two additional resistances arise. The first is commonly known as "access" resistance [44,84–86]. This resistance describes how electric field lines focus from an infinitely large reservoir into a smaller area. This resistance has recently been modeled to account for reservoirs of a finite size where the electric field lines are no longer axisymmetric and are highly influenced by the boundaries (i.e., walls, as in the case of microchannels [83], or planes of symmetry, as in the case of nanochannel arrays [87]). The generalized "access resistances" have been termed "field-focusing" resistances,

$\tilde{R}_{ff}$ [67,68,83]. In this new model, the reservoir geometric lengths are finite. This leads to non-negligible resistances. This is the second resistance – the microchannel resistance, $\tilde{R}_{micro}$.

It is common to assume that the microchannel and field-focusing resistances are negligible relative to the nanochannel resistance. However, as it turns out, such an assumption is inherently wrong. Instead, at low concentrations, these two newer resistances dominate over the nanochannel resistance. In dimensional form, both the microchannel and field-focusing resistances are inversely proportional to the concentration $(\tilde{R}_{micro} \sim \tilde{R}_{ff} \sim \tilde{c}_0^{-1})$. Without surface charge regulation, the nanochannel resistance is a constant that is independent of the concentration. Thus, the total resistance of the system $\{\tilde{R}_{total} \sim (\tilde{R}_{nano} + 2\tilde{R}_{micro} + 2\tilde{R}_{ff})$ – see Ref. [68] for an exact expression$\}$ is dominated by the microchannel and field focusing resistances. The conductance of the system, which is reciprocal to the resistance $(\tilde{G}_{total} = \tilde{R}_{total}^{-1})$, is then determined by $\tilde{R}_{micro}$ and/or $\tilde{R}_{ff}$ such that the conductance is linear with the concentration $(\tilde{G}_{total} \sim \tilde{c}_0)$. This is the dashed red line in **Figure 8**.

Notably, the derivation in Ref. [68] for $\tilde{R}_{total}$ is not limited solely to $\tilde{\sigma}_{s,0}$. The derivation in Ref. [68] also uses the average excess counterion concentration [Eq. (36)] which generally holds for any surface charge density [Eqs. (72)-(74)]. Hence, it can be shown that when the surface charge density is regulated and microchannel effects are accounted for, the conductance as given by Ref. [68] has two inflections – this is the solid purple line in **Figure 8**. Initially, as the concentration is decreased, the slope reduces from 1 to α where the slope is determined by surface charge regulation. Upon further decreasing the concentration, the slope returns to a value of 1 dictated by the microchannel and field focusing resistances. Consider again the work of Smeets et al. [72], who first observed a change in the slope with the concentration. Their system, which was relatively short, should have had strong access resistances effects. However,

the access resistance slope of 1 was not observed. This can be due to the fact that their channel, comprised of silicon nitride, has a different surface charge chemistry (i.e., different charging mechanism). Another possibility lies in the interplay between the nanopore resistance and access resistance. Specifically, the low concentration domain, where surface charge effects are important, can be divided into two. At the upper end of this region (i.e., intermediate concentrations, one finds that the slope is still determined by the nanochannel and the regulated surface charge density such that slope is α. When one goes down to lower concentrations, the access resistance which scales with the bulk concentration is larger than the nanochannel resistance the slope is determined by the access resistance such that the slope is once more one – this is the solid purple line in **Figure 8**. In reality, when surface charge regulation occurs, it can experimentally difficult to access the very low concentration regime where the slope is 1 because the region of intermediate concentration is sufficiently large.

In contrast to this work, the solution of Ref. [68], which accounts for the microchannels, does not account for the effects of convection and slip. Future works should consider field focusing resistances combined with convective effects as well as with hydrodynamic slip.

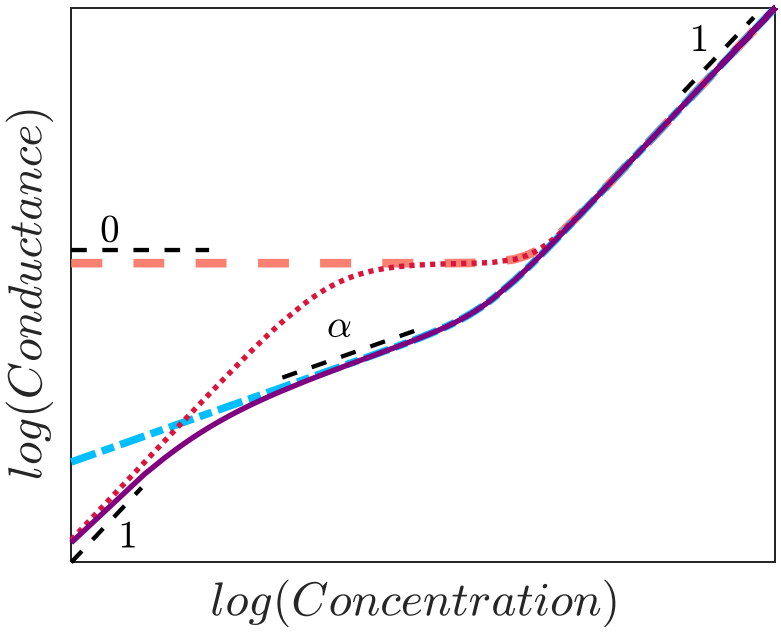

Figure 8. Schematic behavior of the linear Ohmic conductance, G , of a *nanochannel-microchannel* system versus the bulk concentration, c_0. The two lines of the nanochannel-only system (shown in **Figure 1**) have been added for comparison's sake.

In this work, we have focused on systems that have large aspect ratios $(L/a \gg 1)$. However, in recent years, we have seen the advancement of ion transport systems based on 2D materials whereby the system's thickness is of the order of the radius $(L/a \sim 1)$ or smaller $(L/a \ll 1)$. Future works should undoubtedly focus on these systems. However, in such systems, the lack of fully-developed profiles will undoubtedly result in more complicated mathematics and physics.

In conclusion, in this work, we have delineated the interplay of surface charge regulation, convection, and slip lengths on the slope of the conductance. The results of this work can be used to improve the design stages of electro-kinetically based nanofluidics systems.

ACKNOWLEDGEMENTS

We thank Mr. John Sebastian for proofreading this work. This work was supported by the Israel Science Foundation (Grant Nos. 337/20 and 1953/20). We thank the Ilse Katz Institute for Nanoscale Science & Technology for their support.

APPENDIX A: DERIVATION OF EQ. (2)

Here we will show how to derive Eq. (2) for the case of no convection when the electrolyte is symmetric and at its two ends are bulk reservoirs. The possible inclusion of the advective term and its effects are also discussed. This approach can be generalized for non-symmetric electrolytes. Also, this derivation is a simplified derivation relative to the derivation that accounts for the effects of the microchannel (including access/field-focusing resistances).

For an axisymmetric system, when $\partial_\theta = 0$, the 2D Poisson equation [Eq. (7)] is given by

$$\nabla^2 \vartheta = \frac{(r\varphi_{,r})_{,r}}{r} + \vartheta_{,xx} = \frac{-(c_+ - c_-)}{2\varepsilon^2}. \tag{84}$$

We apply the cross-sectional average [Eq. (34)] to this equation. The radial-dependent term is

$$\overline{\frac{(r\varphi_{,r})_{,r}}{r}} = 2\int_0^1 \frac{(r\varphi_{,r})_{,r}}{r} r dr = 2\int_0^1 (r\varphi_{,r})_{,r} dr = 2(r\varphi_{,r})\Big|_0^1 = 2\sigma_s. \tag{85}$$

We have utilized the boundary conditions given by Eqs. (21)-(22) we insert this and find that

$$2\sigma_s + \overline{\vartheta}_{,xx} = \frac{-(\overline{c}_+ - \overline{c}_-)}{2\varepsilon^2} \Rightarrow \overline{\vartheta}_{,xx} = \frac{-(\overline{c}_+ - \overline{c}_- - N)}{2\varepsilon^2}. \tag{86}$$

where $N = -4\sigma_s\varepsilon^2$ is once more Eq. (35). Once more, we can consider a linear potential drop $\vartheta(r,x) = V(1-x/L)$ [similar to Eq. (14)]. Note that the Laplacian of such a potential is zero. We find the expected difference between the counterions and coions is precisely the value of the average excess counterion concentration

$$\overline{c}_+ - \overline{c}_- = N \Rightarrow c_+ = c_- + N = c + N. \tag{87}$$

Note that the difference between the counterion and coions holds for all concentrations (or all values of N).

We now consider the Nernst-Planck equations (for the sake of simplifying notations, we drop the $\pm$ subscripts for the following two equations)

$$-\nabla \cdot \mathbf{j} = \nabla \cdot \{j_r, j_\theta, j_x\} = (rj_r)_{,r} + j_{x,x} = 0. \tag{88}$$

Applying cross-sectional average and utilizing Eqs. (18) leads to

$$\overline{(rj_r)_{,r}} + \overline{j}_{x,x} = 0 \Rightarrow (rj_r)\Big|_0^1 + \overline{j}_{x,x} = 0 \Rightarrow \overline{j}_{x,x} = 0 \Rightarrow \overline{j}_x = const. \tag{89}$$

We find that each of the fluxes are given by constants. We now consider both the positive and negative species

$$-\overline{j}_\pm = \overline{c}_{\pm,z} \pm \overline{c_\pm \vartheta_{,x}} - \mathrm{Pe}\overline{u_x\, c_\pm}. \tag{90}$$

838 In general, the average of a multiplication of functions is not equal to the multiplication of the
839 averages. For the electro-migrative term, we note that $\vartheta_{,x} = -V/L$ so that $\overline{c_\pm \vartheta_{,x}} = \overline{c}_\pm \overline{\vartheta}_{,x}$.
840 However, this is a degenerate case. In contrast, $\overline{u_x\, c_\pm} \neq \overline{u}_x\, \overline{c}_\pm$ (discussed thoroughly in
841 Ref. [58]). As noted in the main text, the model for u_x and $c_\pm$ varies substantially from the
842 two limits of $N \gg 1$ and $N \ll 1$. A uniform solution for all these functions is not known for all
843 concentrations – this is related to finding a solution for the Poisson-Boltzmann at all
844 concentrations. Thus the expression for $\overline{u_x\, c_\pm}$ is highly dependent on whether $N \gg 1$ or $N \ll 1$
845 . In the following, we will neglect the effects of convection. We have

846 $$-\overline{j}_\pm = \overline{c}_{\pm,z} \mp \overline{c}_\pm V/L\,. \tag{91}$$

847 We take the difference between these two equations from which we find a relation between the
848 electrical current density and the voltage drop and insert Eq. (87)

849 $$\overline{i} = \overline{j}_+ - \overline{j}_- = (2\overline{c} + N)V/L\,. \tag{92}$$

850 To find $\overline{c}$, we utilize the electrochemical potential $\overline{\mu}_\pm = \ln \overline{c}_\pm \pm \overline{\phi}$ and require that this term is
851 continuous at the edges of the system ($x = 0, L$). We note that the sum of the positive and
852 negative electrochemical potentials can be written as $\overline{\mu} = \ln(\overline{c}_+ \overline{c}_-)$. As noted in the following
853 appendix, in the reservoirs, we have uniform bulk concentrations $(c = 1)$

854 $$\overline{\mu}_{reservoirs} = \mu_{nano} \Rightarrow (\overline{c}_+ \overline{c}_-)_{nano} = 1 \Rightarrow \overline{c}(\overline{c} + N) = 1. \tag{93}$$

855 The leads to

856 $$\overline{c} = -\frac{N}{2} + \sqrt{\frac{N^2}{4} + 1}\,. \tag{94}$$

857 Inserting this into Eq. (92)

858 $$G = \frac{\overline{i}}{V} = \frac{1}{L}\sqrt{\frac{N^2}{4} + 1}\,. \tag{95}$$

Upon re-dimensionalization, we recover Eq. (2). In this derivation, we have only assumed the system can be characterized by cross-sectional averages. Notably, we utilize the average of the excess counterion concentrations, N. We see that that this equation can be divided into the two limits of vanishing $(N \ll 1)$ and high selectivity $(N \gg 1)$

$$G = \begin{cases} G_{vanishing}(N \ll 1) = L^{-1} \\ G_{high}(N \gg 1) = \frac{1}{2} NL^{-1} \end{cases}. \tag{96}$$

Classically, it is thought that σ_s (or N) is spatially constant. Indeed this must be a spatial constant, but that doesn't prohibit σ_s from being concentration-dependent. Thus, this classical approach, which holds for all concentrations, can also account for space charge regulation.

If one were to add advection, the resultant solution would change drastically. However, the general expression for the advective current is not known for all N, and thus we are limited to $N \ll 1$ and $N \gg 1$. In particular, this work focuses on $N \gg 1$ which is by far more relevant to nanochannels.

Also, as noted above, we have assumed that $c_{reservoirs} = 1$. However, this assumption can also be alleviated so that we consider the effects of the microchannels. This approach is discussed thoroughly in Ref. [68].

APPENDIX B: NUMERICAL SIMULATIONS

Equations (6)-(9) are numerically solved using COMSOL in the 2D axisymmetric geometry specified in **Figure 9**. Specifically, the Transport of Diluted Species, Electro-static, and Creeping Flow modules are used for a cylinder whose non-dimensional radius is $a = 1$ and length $L = 10^4$. We have utilized $L/a \ggg 1$ to ensure that the profiles are fully developed. For the ionic fluxes, we utilize the no-flux BC [Eq. (18)] at the wall, a symmetry BC at the center of the channel $[\mathbf{j}_{\pm}(r = 0) \cdot \hat{\mathbf{r}} = 0]$, and bulk concentrations at the two ends $c_{\pm}(x = 0, L) = 1$

. For the electric potential, we use the symmetry and surface charge conditions given by Eqs. (21)-(22), respectively. Specifically, for the surface charge density we have used Eqs. (69)-(71) . Additionally, we have a potential drop of V across the system whereby $\vartheta(x=0)=V$ and $\vartheta(x=L)=0$. For fluid flow, we utilized the symmetry and slip boundary conditions given in Eqs. (29)-(30), respectively. At the two ends of the channel, we used inlet and outlet BCs whereby the normal stresses were zero, and the pressures were defined as zero. The lack of a pressure difference across the two ends ensures that the pressure gradient is zero in the fully developed region.

For the convection-less scenario, we used $\mathrm{Pe}=0$ while for the convection scenario, we used the value given by Eq. (13) and the parameter values given in **Table 1**. The slip length b was varied from the case of no-slip $(b=0)$ up to $b=10$. In all the various scenarios, to simulate the change in concentration, we varied the non-dimensional EDL [Eq. (11)]. Simulating three order of magnitude difference in ε corresponds to six orders of magnitudes in concentrations.

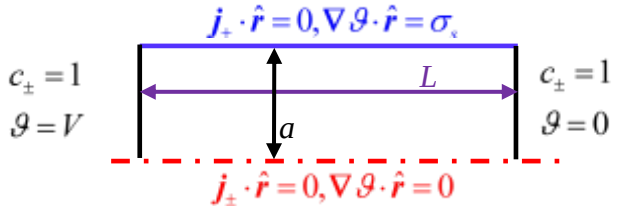

Figure 9. Two-dimensional axisymmetric geometry used for numerical simulations. The bottom dashed red line is the line of symmetry $r=0$. The top solid blue line is the cylinder surface located at $r=a=1$. The two vertical black lines are the bulk reservoirs located at $x=0$ and $x=L$.

Table 2 provides the dimensional parameters used for the figures in the main text. **Table 3** provides a list of important normalization factors

Table 1. Non-dimensional parameters used in simulations

	Notation	**Value**
Radius	a	1
Length	L	10^4
Potential Drop	V	1

Surface charge without SCR	$\gamma = -(\tilde{\sigma}_{s,0} / \tilde{\sigma}_d)$	10
Exponent of *p*K and *p*H[1]	$\beta = 10^{\mathrm{pK-pH}_\infty}$	1
Surface charge with SCR	$(\tilde{\sigma}_{s,\frac{1}{2}} / \tilde{\sigma}_d) = -\frac{1}{2}[\gamma / (\beta\varepsilon^2)]^{1/2}$	$-\frac{1}{2}(10/\varepsilon^2)^{1/2}$
Surface charge with SCR	$(\tilde{\sigma}_{s,\frac{1}{3}} / \tilde{\sigma}_d) = -[\gamma / (\beta\varepsilon^2)]^{1/3}$	$-(10/\varepsilon^2)^{1/3}$
Non-dimensional EDL	ε	$[10^{-2},10]$
Valency	z	1
Relative permittivity	ε_r	78
Peclet number	$\mathrm{Pe} = \tilde{\varepsilon}_0\varepsilon_r\tilde{\varphi}_{th}^2 / (\tilde{\mu}\tilde{D})$	0.4554

[1] This particular value of $\mathrm{pK} - \mathrm{pH}_\infty = 0$ was chosen for numerical convenience.

Table 2. Dimensional parameters used for presentation purposes. All units are given in SI units.

	Notation	**Value**
Diffusion coefficient	$\tilde{D}$	$10^{-9}[\mathrm{m^2 s^{-1}}]$
Nanopore radius	$\tilde{a}$	$10^{-8}[\mathrm{m}]$
Temperature	$\tilde{T}$	298[K]
Viscosity	$\tilde{\mu}$	$10^{-3}[\mathrm{Pa\times s}]$

Table 3. List of important normalization factors.

	Notation	**Value**
Thermal potential	$\tilde{\varphi}_{th} = \tilde{\vartheta}_{th} = \tilde{R}_g\tilde{T} / \tilde{F}z$	25.7 [mV]
Surface charge	$\tilde{\sigma}_d = \tilde{\varepsilon}_0\varepsilon_r\tilde{\varphi}_{th} / \tilde{a}$	$1.8\times10^{-3}[\mathrm{C/m^2}]$

REFERENCES

[1] J. P. Thiruraman, P. Masih Das, and M. Drndić, *Ions and Water Dancing through Atom-Scale Holes: A Perspective toward "Size Zero,"* ACS Nano **14**, 3736 (2020).

[2] S. K. Patel, P. M. Biesheuvel, and M. Elimelech, *Energy Consumption of Brackish Water Desalination: Identifying the Sweet Spots for Electrodialysis and Reverse Osmosis*, ACS EST Eng. (2021).

[3] R. H. Tunuguntla, R. Y. Henley, Y.-C. Yao, T. A. Pham, M. Wanunu, and A. Noy, *Enhanced Water Permeability and Tunable Ion Selectivity in Subnanometer Carbon Nanotube Porins*, Science **357**, 792 (2017).

[4] J. K. Holt, H. G. Park, Y. Wang, M. Stadermann, A. B. Artyukhin, C. P. Grigoropoulos, A. Noy, and O. Bakajin, *Fast Mass Transport Through Sub-2-Nanometer Carbon Nanotubes*, Science **312**, 1034 (2006).

[5] S. P. Surwade, S. N. Smirnov, I. V. Vlassiouk, R. R. Unocic, G. M. Veith, S. Dai, and S. M. Mahurin, *Water Desalination Using Nanoporous Single-Layer Graphene*, Nature Nanotechnology **10**, 459 (2015).

[6] J. Feng, M. Graf, K. Liu, D. Ovchinnikov, D. Dumcenco, M. Heiranian, V. Nandigana, N. R. Aluru, A. Kis, and A. Radenovic, *Single-Layer MoS_2 Nanopores as Nanopower Generators*, Nature **536**, 197 (2016).

[7] C. Chen and L. Hu, *Nanoscale Ion Regulation in Wood-Based Structures and Their Device Applications*, Advanced Materials **33**, 2002890 (2021).

[8] L. Bocquet, *Nanofluidics Coming of Age*, Nat. Mater. **19**, 3 (2020).

[9] N. Kavokine, R. R. Netz, and L. Bocquet, *Fluids at the Nanoscale: From Continuum to Subcontinuum Transport*, Annu. Rev. Fluid Mech. (2020).

[10] A. Siria, P. Poncharal, A.-L. Biance, R. Fulcrand, X. Blase, S. T. Purcell, and L. Bocquet, *Giant Osmotic Energy Conversion Measured in a Single Transmembrane Boron Nitride Nanotube*, Nature **494**, 455 (2013).

[11] A. Siria, M.-L. Bocquet, and L. Bocquet, *New Avenues for the Large-Scale Harvesting of Blue Energy*, Nature Reviews Chemistry **1**, 11 (2017).

[12] L. Ding, D. Xiao, Z. Lu, J. Deng, Y. Wei, J. Caro, and H. Wang, *Oppositely Charged Ti3C2Tx MXene Membranes with 2D Nanofluidic Channels for Osmotic Energy Harvesting*, Angewandte Chemie **132**, (2020).

[13] S. Hong, F. Ming, Y. Shi, R. Li, I. S. Kim, C. Y. Tang, H. N. Alshareef, and P. Wang, *Two-Dimensional Ti3C2Tx MXene Membranes as Nanofluidic Osmotic Power Generators*, ACS Nano **13**, 8917 (2019).

[14] Z. Zhang, S. Yang, P. Zhang, J. Zhang, G. Chen, and X. Feng, *Mechanically Strong MXene/Kevlar Nanofiber Composite Membranes as High-Performance Nanofluidic Osmotic Power Generators*, Nat Commun **10**, 1 (2019).

[15] W. Xin, Z. Zhang, X. Huang, Y. Hu, T. Zhou, C. Zhu, X.-Y. Kong, L. Jiang, and L. Wen, *High-Performance Silk-Based Hybrid Membranes Employed for Osmotic Energy Conversion*, Nat Commun **10**, 1 (2019).

[16] L.-J. Cheng and L. J. Guo, *Rectified Ion Transport through Concentration Gradient in Homogeneous Silica Nanochannels*, Nano Lett. **7**, 3165 (2007).

[17] Q.-Y. Wu, C. Wang, R. Wang, C. Chen, J. Gao, J. Dai, D. Liu, Z. Lin, and L. Hu, *Salinity-Gradient Power Generation with Ionized Wood Membranes*, Advanced Energy Materials **10**, 1902590 (2020).

[18] Y. Green, Y. Edri, and G. Yossifon, *Asymmetry-Induced Electric Current Rectification in Permselective Systems*, Phys. Rev. E **92**, 033018 (2015).

[19] D. Brogioli, *Extracting Renewable Energy from a Salinity Difference Using a Capacitor*, Phys. Rev. Lett. **103**, 058501 (2009).

[20] F. La Mantia, M. Pasta, H. D. Deshazer, B. E. Logan, and Y. Cui, *Batteries for Efficient Energy Extraction from a Water Salinity Difference*, Nano Lett. **11**, 1810 (2011).

[21] F. H. J. van der Heyden, D. J. Bonthuis, D. Stein, C. Meyer, and C. Dekker, *Power Generation by Pressure-Driven Transport of Ions in Nanofluidic Channels*, Nano Lett. **7**, 1022 (2007).

[22] D. Branton, D. W. Deamer, A. Marziali, H. Bayley, S. A. Benner, T. Butler, M. Di Ventra, S. Garaj, A. Hibbs, X. Huang, S. B. Jovanovich, P. S. Krstic, S. Lindsay, X. S. Ling, C. H. Mastrangelo, A. Meller, J. S. Oliver, Y. V. Pershin, J. M. Ramsey, R. Riehn, G. V. Soni, V. Tabard-Cossa, M. Wanunu, M. Wiggin, and J. A. Schloss, *The Potential and Challenges of Nanopore Sequencing*, Nat Biotech **26**, 1146 (2008).

[23] A. Meller, L. Nivon, and D. Branton, *Voltage-Driven DNA Translocations through a Nanopore*, Phys. Rev. Lett. **86**, 3435 (2001).

[24] B. Nadler, Z. Schuss, U. Hollerbach, and R. S. Eisenberg, *Saturation of Conductance in Single Ion Channels: The Blocking Effect of the near Reaction Field*, Phys. Rev. E **70**, 051912 (2004).

[25] A. Meller, *A New Tool for Cell Signalling Research*, Nat. Nanotechnol. **14**, 732 (2019).

[26] M. Aramesh, C. Forró, L. Dorwling-Carter, I. Lüchtefeld, T. Schlotter, S. J. Ihle, I. Shorubalko, V. Hosseini, D. Momotenko, T. Zambelli, E. Klotzsch, and J. Vörös, *Localized Detection of Ions and Biomolecules with a Force-Controlled Scanning Nanopore Microscope*, Nat. Nanotechnol. **14**, 791 (2019).

[27] M. Wanunu, W. Morrison, Y. Rabin, A. Y. Grosberg, and A. Meller, *Electrostatic Focusing of Unlabelled DNA into Nanoscale Pores Using a Salt Gradient*, Nature Nanotechnology **5**, 160 (2010).

[28] M. Wanunu, T. Dadosh, V. Ray, J. Jin, L. McReynolds, and M. Drndić, *Rapid Electronic Detection of Probe-Specific MicroRNAs Using Thin Nanopore Sensors*, Nature Nanotechnology **5**, 807 (2010).

[29] M. Wanunu, J. Sutin, and A. Meller, *DNA Profiling Using Solid-State Nanopores: Detection of DNA-Binding Molecules*, Nano Lett. **9**, 3498 (2009).

[30] Z. S. Siwy and S. Howorka, *Engineered Voltage-Responsive Nanopores*, Chem. Soc. Rev. **39**, 1115 (2010).

[31] R. Karnik, R. Fan, M. Yue, D. Li, P. Yang, and A. Majumdar, *Electrostatic Control of Ions and Molecules in Nanofluidic Transistors*, Nano Lett. **5**, 943 (2005).

[32] R. Karnik, C. Duan, K. Castelino, H. Daiguji, and A. Majumdar, *Rectification of Ionic Current in a Nanofluidic Diode*, Nano Lett. **7**, 547 (2007).

[33] W. Guan, R. Fan, and M. A. Reed, *Field-Effect Reconfigurable Nanofluidic Ionic Diodes*, Nat Commun **2**, 506 (2011).

[34] R. Yan, W. Liang, R. Fan, and P. Yang, *Nanofluidic Diodes Based on Nanotube Heterojunctions*, Nano Lett. **9**, 3820 (2009).

[35] I. Vlassiouk, S. Smirnov, and Z. Siwy, *Nanofluidic Ionic Diodes. Comparison of Analytical and Numerical Solutions*, ACS Nano **2**, 1589 (2008).

[36] I. Vlassiouk, T. R. Kozel, and Z. S. Siwy, *Biosensing with Nanofluidic Diodes*, J. Am. Chem. Soc. **131**, 8211 (2009).

[37] Y. Green, *Current-Voltage Response for Unipolar Funnel-Shaped Nanochannel Diodes*, Phys. Rev. E **98**, 033114 (2018).

[38] R. Abu-Rjal and Y. Green, *Bipolar Nanochannels: A Systematic Approach to Asymmetric Problems*, ACS Appl. Mater. Interfaces **13**, 27622 (2021).

[39] R. A. Lucas and Z. S. Siwy, *Tunable Nanopore Arrays as the Basis for Ionic Circuits*, ACS Appl. Mater. Interfaces **12**, 56622 (2020).

[40] Z. Sarkadi, D. Fertig, Z. Ható, M. Valiskó, and D. Boda, *From Nanotubes to Nanoholes: Scaling of Selectivity in Uniformly Charged Nanopores through the Dukhin Number for 1:1 Electrolytes*, J. Chem. Phys. **154**, 154704 (2021).

[41] M. Valiskó, B. Matejczyk, Z. Ható, T. Kristóf, E. Mádai, D. Fertig, D. Gillespie, and D. Boda, *Multiscale Analysis of the Effect of Surface Charge Pattern on a Nanopore's Rectification and Selectivity Properties: From All-Atom Model to Poisson-Nernst-Planck*, J. Chem. Phys. **150**, 144703 (2019).

[42] Y. Qiu, R. A. Lucas, and Z. S. Siwy, *Viscosity and Conductivity Tunable Diode-like Behavior for Meso- and Micropores*, J. Phys. Chem. Lett. **8**, 3846 (2017).

[43] T. Plett, M. L. Thai, J. Cai, I. Vlassiouk, R. M. Penner, and Z. S. Siwy, *Ion Transport in Gel and Gel–Liquid Systems for LiClO4-Doped PMMA at the Meso- and Nanoscales*, Nanoscale **9**, 16232 (2017).

[44] A. Alcaraz, M. L. López, M. Queralt-Martín, and V. M. Aguilella, *Ion Transport in Confined Geometries below the Nanoscale: Access Resistance Dominates Protein Channel Conductance in Diluted Solutions*, ACS Nano **11**, 10392 (2017).

[45] M. Queralt-Martín, M. L. López, M. Aguilella-Arzo, V. M. Aguilella, and A. Alcaraz, *Scaling Behavior of Ionic Transport in Membrane Nanochannels*, Nano Lett. **18**, 6604 (2018).

[46] S. Faucher, N. Aluru, M. Z. Bazant, D. Blankschtein, A. H. Brozena, J. Cumings, J. Pedro de Souza, M. Elimelech, R. Epsztein, J. T. Fourkas, A. G. Rajan, H. J. Kulik, A. Levy, A. Majumdar, C. Martin, M. McEldrew, R. P. Misra, A. Noy, T. A. Pham, M. Reed, E. Schwegler, Z. Siwy, Y. Wang, and M. Strano, *Critical Knowledge Gaps in Mass Transport through Single-Digit Nanopores: A Review and Perspective*, J. Phys. Chem. C **123**, 21309 (2019).

[47] L. Wang, Z. Wang, S. K. Patel, S. Lin, and M. Elimelech, *Nanopore-Based Power Generation from Salinity Gradient: Why It Is Not Viable*, ACS Nano **15**, 4093 (2021).

[48] H. B. Park, J. Kamcev, L. M. Robeson, M. Elimelech, and B. D. Freeman, *Maximizing the Right Stuff: The Trade-off between Membrane Permeability and Selectivity*, Science **356**, (2017).

[49] N. W. Ashcroft and N. D. Mermin, *Solid State Physics*, 1 edition (Cengage Learning, New York, 1976).

[50] D. Stein, M. Kruithof, and C. Dekker, *Surface-Charge-Governed Ion Transport in Nanofluidic Channels*, Phys. Rev. Lett. **93**, 035901 (2004).

[51] L. Bocquet and E. Charlaix, *Nanofluidics, from Bulk to Interfaces*, Chemical Society Reviews **39**, 1073 (2010).

[52] G. Yossifon and H.-C. Chang, *Changing Nanoslot Ion Flux with a Dynamic Nanocolloid Ion-Selective Filter: Secondary Overlimiting Currents Due to Nanocolloid-Nanoslot Interaction*, Phys. Rev. E **81**, 066317 (2010).

[53] R. B. Schoch, J. Han, and P. Renaud, *Transport Phenomena in Nanofluidics*, Rev. Mod. Phys. **80**, 839 (2008).

[54] E. Secchi, A. Niguès, L. Jubin, A. Siria, and L. Bocquet, *Scaling Behavior for Ionic Transport and Its Fluctuations in Individual Carbon Nanotubes*, Phys. Rev. Lett. **116**, 154501 (2016).

[55] P. M. Biesheuvel and M. Z. Bazant, *Analysis of Ionic Conductance of Carbon Nanotubes*, Phys. Rev. E **94**, 050601 (2016).

[56] Y. Uematsu, R. R. Netz, L. Bocquet, and D. J. Bonthuis, *Crossover of the Power-Law Exponent for Carbon Nanotube Conductivity as a Function of Salinity*, J. Phys. Chem. B **122**, 2992 (2018).

[57] M. Manghi, J. Palmeri, K. Yazda, F. Henn, and V. Jourdain, *Role of Charge Regulation and Flow Slip in the Ionic Conductance of Nanopores: An Analytical Approach*, Phys. Rev. E **98**, 012605 (2018).

[58] Y. Green, *Ion Transport in Nanopores with Highly Overlapping Electric Double Layers*, J. Chem. Phys. **154**, 084705 (2021).

[59] M. Biesheuvel and Jouke. E. Dykstra, *Physics of Electrochemical Processes*, Pre-release (www.physicsofelectrochemicalprocesses.com, 2020).

[60] O. Schnitzer and E. Yariv, *Electric Conductance of Highly Selective Nanochannels*, Phys. Rev. E **87**, 054301 (2013).

[61] H. J. M. Hijnen, J. van Daalen, and J. A. M. Smit, *The Application of the Space-Charge Model to the Permeability Properties of Charged Microporous Membranes*, Journal of Colloid and Interface Science **107**, 525 (1985).

[62] *We Thank the Anonymous Referee for Referring Us to the Work of Hijnen et al. [XX] of Which We Were Unfamiliar With.*

[63] K. Yazda, S. Tahir, T. Michel, B. Loubet, M. Manghi, J. Bentin, F. Picaud, J. Palmeri, F. Henn, and V. Jourdain, *Voltage-Activated Transport of Ions through Single-Walled Carbon Nanotubes*, Nanoscale **9**, 11976 (2017).

[64] S. Balme, F. Picaud, M. Manghi, J. Palmeri, M. Bechelany, S. Cabello-Aguilar, A. Abou-Chaaya, P. Miele, E. Balanzat, and J. M. Janot, *Ionic Transport through Sub-10 Nm Diameter Hydrophobic High-Aspect Ratio Nanopores: Experiment, Theory and Simulation*, Sci Rep **5**, 10135 (2015).

[65] O. I. Vinogradova, E. F. Silkina, and E. S. Asmolov, *Enhanced Transport of Ions by Tuning Surface Properties of the Nanochannel*, ArXiv:2106.07915 [Cond-Mat, Physics:Physics] (2021).

[66] Y. Green, *Conditions for Electroneutrality Breakdown in Nanopores*, J. Chem. Phys. **155**, 184701 (2021).

[67] Y. Green, R. Eshel, S. Park, and G. Yossifon, *Interplay between Nanochannel and Microchannel Resistances*, Nano Lett. **16**, 2744 (2016).

[68] Y. Green, R. Abu-Rjal, and R. Eshel, *Electrical Resistance of Nanochannel-Microchannel Systems: An Exact Solution*, Phys. Rev. Applied **14**, 014075 (2020).

[69] R. B. Schoch and P. Renaud, *Ion Transport through Nanoslits Dominated by the Effective Surface Charge*, Applied Physics Letters **86**, 253111 (2005).

[70] R. B. Schoch, H. van Lintel, and P. Renaud, *Effect of the Surface Charge on Ion Transport through Nanoslits*, Physics of Fluids **17**, 100604 (2005).

[71] H. Wang, L. Su, M. Yagmurcukardes, J. Chen, Y. Jiang, Z. Li, A. Quan, F. M. Peeters, C. Wang, A. K. Geim, and S. Hu, *Blue Energy Conversion from Holey-Graphene-like Membranes with a High Density of Subnanometer Pores*, Nano Lett. **20**, 8634 (2020).

[72] R. M. M. Smeets, U. F. Keyser, D. Krapf, M.-Y. Wu, N. H. Dekker, and C. Dekker, *Salt Dependence of Ion Transport and DNA Translocation through Solid-State Nanopores*, Nano Lett. **6**, 89 (2006).

[73] Y.-C. Yao, A. Taqieddin, M. A. Alibakhshi, M. Wanunu, N. R. Aluru, and A. Noy, *Strong Electroosmotic Coupling Dominates Ion Conductance of 1.5 Nm Diameter Carbon Nanotube Porins*, ACS Nano **13**, 12851 (2019).

[74] Y. Noh and N. R. Aluru, *Ion Transport in Electrically Imperfect Nanopores*, ACS Nano **14**, 10518 (2020).

[75] P. B. Peters, R. van Roij, M. Z. Bazant, and P. M. Biesheuvel, *Analysis of Electrolyte Transport through Charged Nanopores*, Phys. Rev. E **93**, 053108 (2016).

[76] E. Secchi, S. Marbach, A. Niguès, D. Stein, A. Siria, and L. Bocquet, *Massive Radius-Dependent Flow Slippage in Carbon Nanotubes*, Nature **537**, 210 (2016).

[77] Q. Xie, M. A. Alibakhshi, S. Jiao, Z. Xu, M. Hempel, J. Kong, H. G. Park, and C. Duan, *Fast Water Transport in Graphene Nanofluidic Channels*, Nature Nanotech **13**, 238 (2018).

[78] C. Herrero, G. Tocci, S. Merabia, and L. Joly, *Fast Increase of Nanofluidic Slip in Supercooled Water: The Key Role of Dynamics*, Nanoscale **12**, 20396 (2020).

[79] Y. Xie, L. Fu, T. Niehaus, and L. Joly, *Liquid-Solid Slip on Charged Walls: The Dramatic Impact of Charge Distribution*, Phys. Rev. Lett. **125**, 014501 (2020).

[80] G. J. Wang and N. G. Hadjiconstantinou, *Universal Molecular-Kinetic Scaling Relation for Slip of a Simple Fluid at a Solid Boundary*, Phys. Rev. Fluids **4**, 064201 (2019).

[81] Yoav Green, *Electrical Conductance of Charged Nanopores*, (submitted to Phys. Rev. Lett.).

[82] A. Levy, J. P. de Souza, and M. Z. Bazant, *Breakdown of Electroneutrality in Nanopores*, Journal of Colloid and Interface Science **579**, 162 (2020).

[83] Y. Green, S. Shloush, and G. Yossifon, *Effect of Geometry on Concentration Polarization in Realistic Heterogeneous Permselective Systems*, Phys. Rev. E **89**, 043015 (2014).

[84] J. E. Hall, *Access Resistance of a Small Circular Pore.*, J Gen Physiol **66**, 531 (1975).

[85] C. Lee, L. Joly, A. Siria, A.-L. Biance, R. Fulcrand, and L. Bocquet, *Large Apparent Electric Size of Solid-State Nanopores Due to Spatially Extended Surface Conduction*, Nano Lett. **12**, 4037 (2012).

[86] I. Vlassiouk, S. Smirnov, and Z. Siwy, *Ionic Selectivity of Single Nanochannels*, Nano Lett. **8**, 1978 (2008).

[87] Y. Green, S. Park, and G. Yossifon, *Bridging the Gap between an Isolated Nanochannel and a Communicating Multipore Heterogeneous Membrane*, Phys. Rev. E **91**, 011002 (R) (2015).